Calibration and Testing of Rapid Prototyped Nozzles for Guidance and Control

By

Christopher Tucker Lyne

Thesis

Submitted to the Faculty of the Graduate

School of Vanderbilt University in

partial fulfillment of the requirements

for the degree of

MASTER OF SCIENCE

in

Mechanical Engineering

December 16, 2017

Nashville, Tennessee

Approved:

Amrutur V. Anilkumar, Ph.D.

Robert W. Pitz, Ph.D.

William A. Emfinger, Ph.D.

ACKNOWLEDGEMENTS

I would like to thank my thesis advisor Dr. Amrutur Anilkumar for his encouragement and mentorship over the past few years. I would also like to thank Robin Midget for always being willing to listen and help whenever he was needed. I'm also grateful to Dr. Pitz and Dr. Emfinger for taking the time out of their busy schedules to sit on my committee.

ABSTRACT

Additive manufacturing of plastics, commonly referred to as Rapid Prototyping, is an emerging field with the potential to improve the performance of guidance and control systems for small satellites. Small-scale nozzles for low temperature thrusters can be easily manufactured using rapid prototyping, leading to a reduction in cost compared to traditional manufacturing techniques. This document presents a case study in the design of a cold gas thruster nozzle for guidance and control, and experimentally assesses the performance of the nozzle. Using the coefficient of thrust as a performance metric, a study is conducted to compare the performance of the rapid prototyped nozzle to a comparable machined nozzle. It was shown that the rapid prototyped nozzle outperformed the machined nozzle in all the test cases, and the primary sources of off nominal performance are identified as surface roughness and viscous effects. This favorable performance demonstrates that rapid prototyping is a viable means of prototyping nozzles for guidance and control systems for small satellites, and potentially for fabricating the final hardware for Space applications.

TABLE OF CONTENTS

LIST OF FIGURES

Figure Page

LIST OF TABLES

Table Page

NOMENCLATURE

AM	Additive Manufacturing
RPT	Rapid Prototyping
MECO	Main Engine Cut-Off
CG	Cold Gas
SLS	Selective Laser Sintering
SLM	Selective Laser Melting
SLA	Stereolithography
RCS	Reaction Control System
VADL	Vanderbilt Aerospace Design Laboratory
DAQ	Data Acquisition
ADC	Analog-to-Digital Converter
CFD	Computational Fluid Dynamics

CHAPTER 1

BACKGROUND

This thesis will discuss the motivation and challenges in developing a cold gas propulsion system for roll control of a low-altitude rocket flight project for the 2016-17 NASA Student Launch Competition. In particular, a comparative study on the performance of rapid prototyped (RPT) and machined nozzles for cold gas thrusters will be performed, and the suitability of RPT nozzles will be assessed for broader applications in Space technology.

1.1 Mission Overview

The 2016-17 NASA SL competition called for the active roll control of the launch vehicle during the coasting phase of flight. In order to successfully fulfill the challenge requirements, the rocket must include a control system that detects main engine cutoff (MECO) and waits a pre-determined period before intentionally inducing a roll of the rocket. The control system monitors the angular position of the rocket and determines the correct time to initiate a counter roll so that the rocket makes two full rotations within the allotted experimental time. At apogee, the avionics system deploys a drogue parachute and later the main parachute for safe recovery of the rocket. Figure 1 shows an overview of the launch operations during the flight experiment.

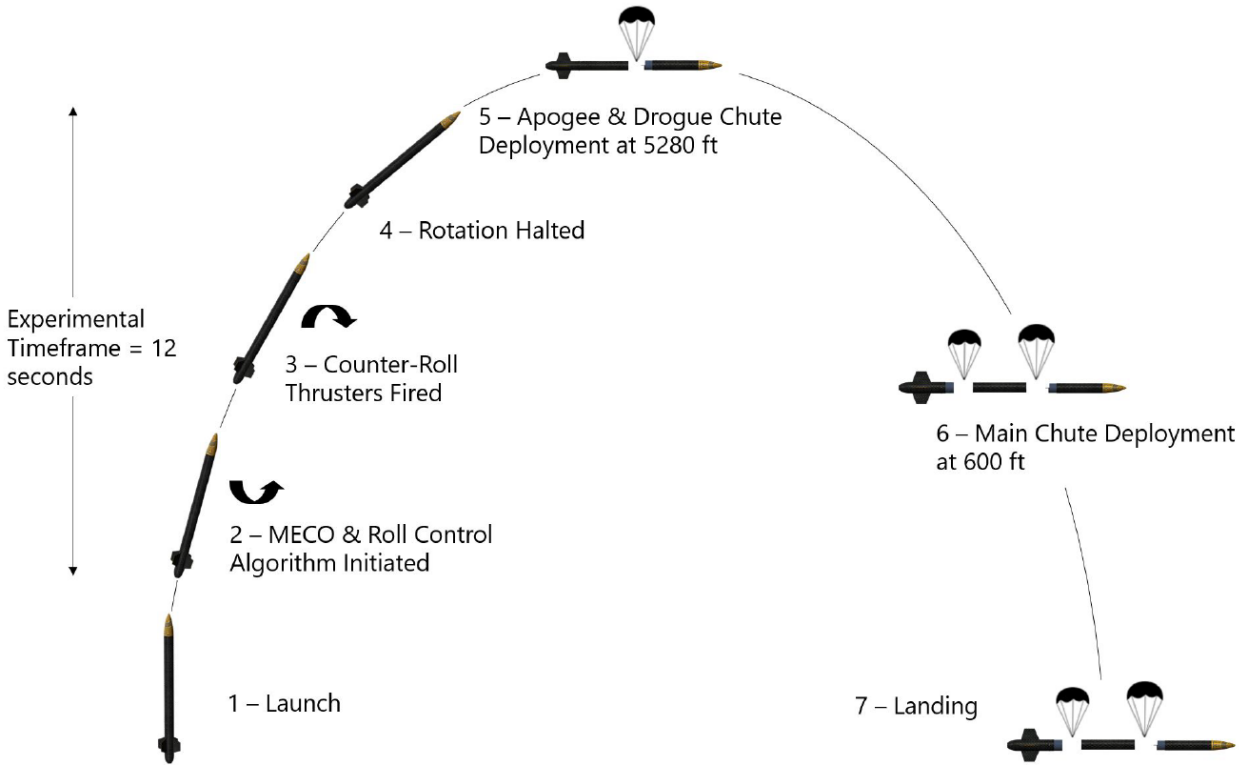

Figure 1: Overview of flight operations

1.2 Design Requirements

During the initial design phase, a set of design requirements was developed to guide the selection of an appropriate rotation control system. The first requirement was to establish a time frame during which the experiment would be conducted. In order to simplify the measurement of angular position, it was decided

that the experiment should be conducted primarily while the rocket is oriented vertically. It is also necessary to wait for a short period after MECO to allow for the rocket to stabilize. These requirements leave an experimental window of approximately 8 seconds. In order to demonstrate robust control of the rocket, a goal was set to complete two rotations in two seconds, followed by 6 seconds of maintaining zero angular velocity. An additional requirement is that the payload system be ground testable, so that systems level integration and performance testing can be conducted prior to the flight experiment. A further requirement is that the system fit into the rocket without exceeding the volume and mass constraints set forth by the rocket size and impulse limits. The final requirements are that the system be non-reactive, safe to develop and operate and fit within the allotted budget.

Considering these requirements, the decision was made to design and build a cold gas (CG) thruster system for roll control. Other candidate systems included a reaction wheel and aerodynamic control surfaces, but were ruled out due to excessive mass and inability to perform reliable ground testing, respectively. Initial calculations were performed to determine the total impulse and thrust requirements for the system (equations 1-8). Approximating the rocket as a solid cylinder with a mass of 15 kg, the moment required to initiate and halt a roll of two rotations in two seconds is 0.46 N-m; the calculation is performed assuming one rotation is completed in 1 second while accelerating, and the remaining rotation is completed in the following second during deceleration. Using the rocket body radius as the effective radius for thrust application and assuming two thrusters for each roll direction, this corresponds to a thrust of 3.3 N each. The total impulse of the CG system is limited to 5% of the solid rocket motor impulse, or 284 N-s. Equation 8 gives the required impulse for the maneuver as 13.2 N-s, falling well below the total impulse limit.

$$\theta = 2\pi\ rad \tag{1}$$

$$\Delta t = 1\ s \tag{2}$$

$$\theta = \frac{1}{2}\alpha t^2 \tag{3}$$

$$\alpha = \frac{2\theta}{t^2} = 4\pi\frac{rad}{s} \tag{4}$$

$$I_\theta = \frac{1}{2}mr^2 = \frac{1}{2}(15\ kg)(0.07\ m)^2 = 0.037\ kg\ m^2 \tag{5}$$

$$T_\theta = I\alpha = (0.037\ kg\ m^2)\left(4\pi\frac{rad}{s}\right) = 0.46\ Nm \tag{6}$$

$$\tau = \frac{0.23\ Nm}{0.07\ m} = 3.3\ N \tag{7}$$

$$I = 2\tau\Delta t = 13.2\ Ns \tag{8}$$

This calculation assumes no flight-based resistive torque on the rocket. In the presence of such a torque the cold gas thrust and time requirement for achieving two complete rotations would increase, but would still be within the capabilities of the thruster design and the rocket flight window as discussed.

1.3 Flight Payload Design

The payload system designed to meet these requirements is shown in figure 2 below. Air is stored in a carbon fiber air tank at 4500 psig and is regulated to a nominal pressure of 450 psig by the attached

pressure regulator. Air is delivered to two sets of thrusters that deliver the roll and counter roll moments. Each thruster set consists of a solenoid valve, and two converging-diverging nozzles that exhaust tangentially out of the rocket body. The payload electronics are located behind the CG system, and are responsible for angular position sensing and controlling the thruster solenoids.

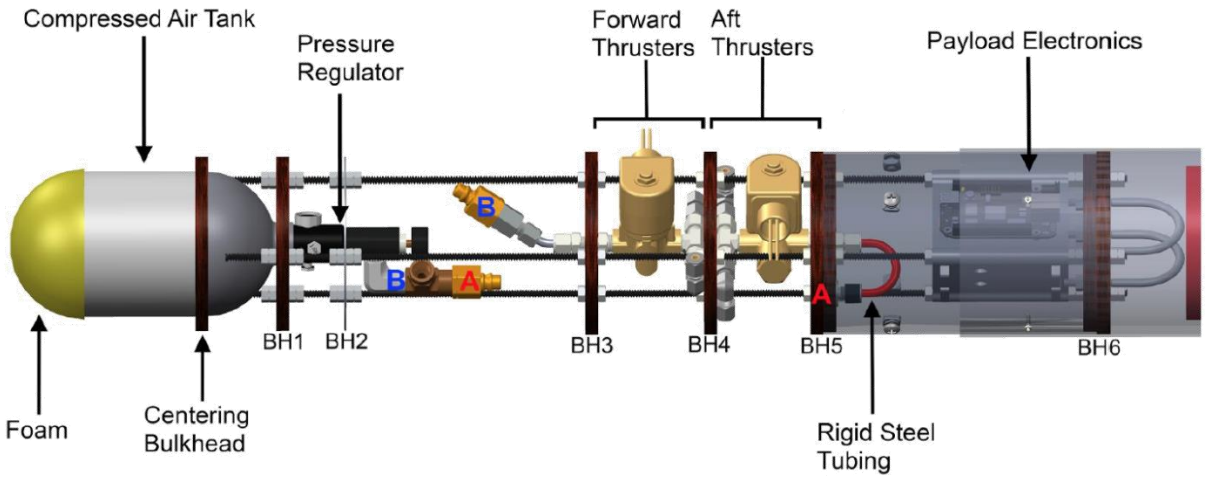

Figure 2: CAD drawing of the Cold Gas Thruster Payload

1.4 Motivation for the Current Study

Although the flight payload performed well, there were considerable difficulties encountered in building the payload as designed. The small dimensions of the nozzles made fabrication difficult, and machining considerations led to a non-ideal nozzle geometry. As a result, performance was sub optimal and considerable time was spent on machining the nozzles for the system. The intent of this study is to present an extension to the work performed for the 2016-17 NASA Student Launch. This study will investigate the feasibility and performance of RPT nozzles for cold gas propulsion systems. The performance of these nozzles will be compared to the nozzles produced by conventional machining processes, and to the limited data on the performance of AM nozzles in the literature. The data resulting from this study will make a considerable contribution to the literature on the performance of AM nozzles, and may be directly applied to the design and fabrication of CG propulsion systems for small satellites.

CHAPTER 2

INTRODUCTION

2.1 Additive Manufacturing in Propulsion

AM is a manufacturing method in which material is added, layer by layer, to build a part. AM contrasts traditional machining processes, which rely on removing material from a solid piece of stock. The advantages of AM include printing complex geometries that are expensive or impossible to fabricate using traditional methods, full automation of the manufacturing process, and the ability to fabricate parts directly from a computer design. This section will discuss the available literature on using AM to produce propulsion systems for satellites and other spacecraft.

2.1.1 Selective Laser Sintering

Several research groups have used an additive manufacturing process called selective laser sintering (SLS) or selective laser melting (SLM) to produce propulsion components for chemical rockets (figure 3). Researchers at the University of Tennessee Knoxville fabricated an Inconel nozzle using SLM and successfully hot fired it for several seconds [1]. NASA has also conducted research on using SLM to manufacture combustion chambers for bipropellant rockets [2]. AM can reduce the expense and complexity of chemical rocket components, allowing monolithic combustion chambers and fuel injector assemblies to be manufactured [2]. The application of AM to the fabrication of propulsion systems can greatly reduce system complexity, reduce cost and manufacturing time, and allow designers to focus on performance and efficient space utilization rather than ease of manufacturing.

Figure 3: Bipropellant combustion chamber printed using SLM [2]

2.1.2 Rapid Prototyping

In low temperature applications, methods other than SLS and SLM may be used to produce parts from thermoplastics. These methods, commonly referred to as rapid prototyping, are substantially less expensive than SLS or SLM, and many universities have RPT equipment readily available. Some investigations into the use of RPT propulsion systems have already been conducted. A group at the University of Vermont fabricated a hydrogen-peroxide thruster for attitude control of a CubeSat using stereolithography, a common rapid prototyping technique [3]. Researchers at Portland State University

used RPT to develop a reaction control system (RCS) for a low-altitude experimental rocket that is capable of producing thrust on the order of 8N [4]. The University of Texas at Austin also rapid prototyped a CG propulsion system to function as an RCS module on the Prox-1 CubeSat, which produced approximately 50mN of thrust [5]. The propellant tank, piping, and nozzles were produced as a monolithic part for the propulsion module, allowing designers to conform to the strict volume limitations of the CubeSat [5].

Rapid prototyping is particularly well suited to manufacturing propulsion systems for small satellites. Because of the strict volume and mass restrictions, small satellites often rely on cold gas propulsion attitude control and small orbital adjustments. It is possible to use RPT to fabricate CG propulsion systems at a fraction of the cost and time of SLS or SLM processes. This opens up the possibility of using RPT in the development and testing, if not final production of CG propulsion systems for small satellites.

Another important application that RPT is particularly well-suited for is in-Space additive manufacturing. Since RPT printers are considerably less complex than printers relying on SLS, they can be smaller and more portable. The raw material can also be stored more easily, often as a liquid prior to printing. Finally, plastics are more easily reprocessed, opening up the possibility of recycling parts printed in space after they are used for the intended purpose.

2.1.3 FormLabs Form 2 Printer

The FormLabs Form 2 printer was used to rapid prototype nozzles for this study. The Form 2 (figure 4) is a consumer 3D printer that uses stereolithography (SLA) to print parts. SLA is a common rapid prototyping technique that works by depositing a thin layer of liquid onto a build platform, then hardening the layer with ultraviolet light to cure the liquid and form a solid layer. SLA can print small, complex parts at a fraction of the cost of SLS or SLM parts. The nozzles for this study were printed with the maximum available resolution (25 microns) using the FormLabs FLGPCL03 material. After printing, the parts were rinsed with isopropyl alcohol to remove uncured resin before use.

Figure 4: FormLabs Form 2 Printer [6]

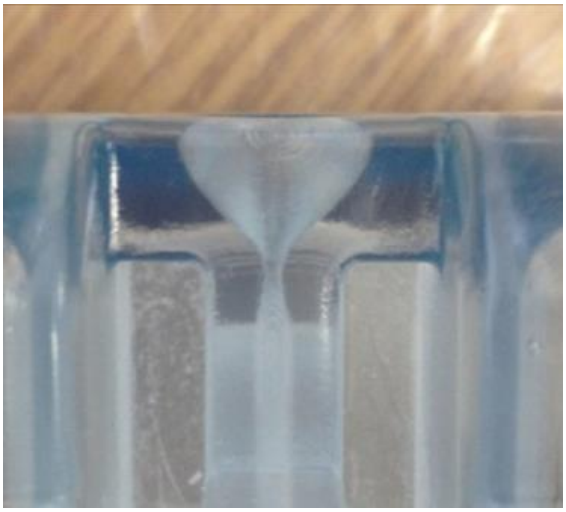

Figure 5: Rapid Prototyped nozzle made using Stereolithography [5]

As of September 2017, the Form 2 has a retail price of approximately $3,500, putting it within the budget of nearly all organizations interested in prototyping or developing guidance and control thrusters for small satellites. Although there are more precise RPT machines available, printing high performance nozzles with the Form 2 will demonstrate that RPT is a viable means of prototyping and manufacture of low-temperature thruster nozzles.

2.1.4 Performance of Additively Manufactured Propulsion Systems

Although a number of groups have used AM to fabricate and test various propulsion modules, relatively little is known about the performance of additively manufactured nozzles compared to those produced using traditional methods. AM can be used to reduce overall system size and greatly reduce the cost of propulsion system development, but designers must know the performance implications of using AM methods if informed design decisions are to be made. Experimental data on the performance of propulsion systems manufactured using SLS is available from [1, 3], but the large dimensions of these systems make the data inapplicable to small satellite propulsion systems. Data on the performance of small-scale propulsion systems is available from [4, 6], but the systems approach to testing is not suitable for studying losses in the nozzle alone. Furthermore, the majority of experimental data was obtained using metallic nozzles fabricated by SLS or SLM and therefore have different surface roughness than the rapid prototyped nozzles commonly used for the fabrication of cold gas propulsion systems.

This study aims to address the lack of experimental data on the performance of RPT nozzles for CG propulsion systems. The nozzles used for this study will be fabricated on low-cost consumer AM equipment commonly available at universities around the country. This approach will better contrast existing studies primarily focused on propulsion systems fabricated using SLS and SLM. The findings of this study will provide much needed information on the suitability of RPT nozzles for cold gas propulsions systems, and will provide information on the use of RPT in the development and fabrication of small satellites.

2.2 Cold Gas Thruster Design Protocol

According to [7], there is a current need for reaction control thrusters with a thrust output of 1-20N to meet the RCS needs for small spacecraft. With this goal in mind, we can consider the other design goals of this study to arrive at an appropriate nozzle design. Since the motivation for the present study is to examine the suitability of nozzles produced by inexpensive additive manufacturing techniques, aspects such as manufacturing precision and material strength must be evaluated. Furthermore, it is important that the dimensions of the printed nozzle are chosen such that a conventional nozzle may be machined and used as a reference for a performance comparison.

2.3 Thrust Stand

In order to reliably study the performance of both the printed and machined nozzles, a high-fidelity thrust stand is needed. In this section, thrust stand designs from the literature will be briefly reviewed to give context to the thrust stand designed and built for this study.

There are a variety of different test stand designs for measuring the thrust output of rocket engines. The thrust response of high thrust engines can typically be measured directly using a load cell, since the thrust output is high relative to the engine weight. For low thrust engines, such as Hall or plasma thrusters, the load cell signal is typically overwhelmed by the weight of the thruster, and the thrust or impulse must be inferred from the motion of a pendulum [8]. Engines that operated in short duration pulses also present their own challenges in thrust and impulse measurement, and typically employ fast-responding piezoelectric sensors for measurement [9].

Numerous thrust stand designs can be found in the literature for the characterization of a wide range of rocket engines and thrusters. State of the art thrust stands designed to characterize electric propulsion devices typically utilize a pendulum-based approach to achieve resolutions in the nano to micro-Newton range [8]. There are three basic types of pendulum based thrust stands: hanging pendulum, inverted pendulum (figure 6), and torsional pendulum (figure 7). Each type consists of a lever arm with the thruster affixed to the end, and a pivot at the other end. When thrust is applied, the arm is free to be displaced and the displacement is measured. Typically, a restraining force is applied via an electromagnetic coil or other device to limit displacement. The thrust is then inferred from a combination of the applied restraining force and displacement measurements.

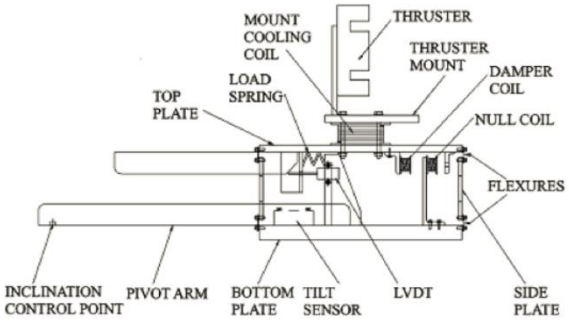

Figure 6: Inverted pendulum design [8]

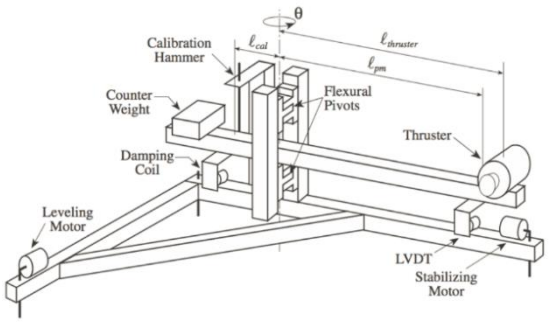

Figure 7: Torsional pendulum design [8]

High thrust measurements are often measured directly using a load cell or piezoelectric transducer (figures 8 and 9). These arrangements tend to be less complex than pendulum based designs, and are desirable if the measured thrust levels are high enough to provide accurate measurements. Piezoelectric sensors (figure 8) are typically used if the thruster is operated in short duration pulses, since these sensors have a fast response time and are usually very stiff and lead to a high resonant frequency for the thrust stand. One such example can be seen in [9], which has a resonant frequency of 1245 Hz and is used for time resolved measurements of short duration pulsed motors. Despite the excellent temporal resolution, the difficulties in building such a system are considerable. The piezoelectric sensors require an extremely high insulation impedance (10^{14} ohms), which is difficult and expensive to realize in practice [9]. A less complex and expensive approach to thrust measurement can be realized through the use of a load cell (figure 9), if the pulse duration of the thruster is sufficiently long. Once such example can be seen in [10], which uses a load cell for thrust measurements of a 5N hydrogen-peroxide monopropellant thruster.

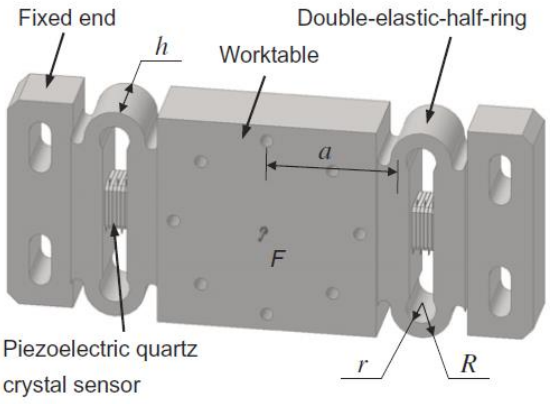

Figure 8: Piezoelectric thrust sensor [9]

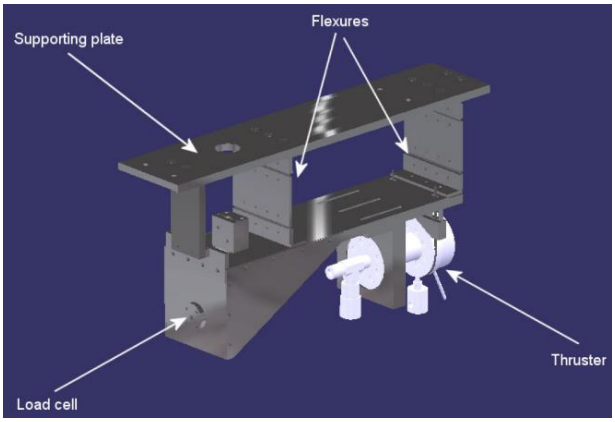

Figure 9: Agostino et al. thrust stand [10]

The thrust stand used in this study was designed for quasi-static measurements of cold gas thrusters in the Newton range, and thus uses a load cell for measurement. The design is loosely based on the thrust stand discussed in [10], with several important modifications. The thrust stand is discussed in detail in section 3.8.

CHAPTER 3

DESIGN PROCEDURE

3.1 Nozzle Theory

The goal of any propulsive system is to produce thrust in order to accelerate the spacecraft. Total thrust can be broken into momentum and pressure components. These two components can be seen in equation 9, which results from a momentum balance conducted on a rocket nozzle [11].

$$\tau = \dot{m}V_e + (P_e - P_a)A_e \tag{9}$$

In order to predict the thrust generated by a nozzle, it is necessary to predict the mass flow rate of propellant ($\dot{m}$), jet exit velocity (V_e), and the exit plane pressure (P_e). It is also necessary to know the ambient pressure that the jet is exposed to (P_a), as well as the exit area of the nozzle (A_e). In the next section, we will develop an analytical framework to predict these values using compressible flow theory.

Nozzle design and performance analysis can be accomplished by considering a simplified model for compressible flow through the nozzle. The assumptions made in the following analysis are:

1. Steady State
2. Quasi One-Dimensional Flow
3. Adiabatic
4. Frictionless
5. Frozen Flow
6. Ideal Gas
7. Axial Exhaust Velocity

The steady state assumption allows us to neglect transient effects in the nozzle, most notably during startup and shut down of the nozzle. Quasi one-dimensional flow refers to flow that only has velocity along the axis of the nozzle, implying that the velocities perpendicular to the nozzle axis are zero. Despite this, the quasi one-dimensional assumption allows for changing cross sectional area available to the flow. The assumptions that the flow is adiabatic and frictionless restrict that the control volume is isolated from heat and momentum exchange with the nozzle walls. The assumption of an ideal gas implies that the specific heat of the gas remains constant.

Under these constraints, we arrive at several important equations in nozzle design [12]. The first key equations to introduce are the stagnation properties. Stagnation conditions refer to the conditions achieved when a flow is stagnated to zero velocity. In isentropic flow, the stagnation pressure and density remain constant throughout the flow field, while in all adiabatic flow the stagnation temperature remains constant. These relations are shown in equations 10 through 12. These equations allow us to calculate the local properties of temperature, pressure, and density in a flow field using the stagnation properties and the local Mach number.

$$\frac{T_0}{T} = 1 + \frac{\gamma - 1}{2}M^2 \tag{10}$$

$$\frac{P_0}{P} = \left(1 + \frac{\gamma - 1}{2}M^2\right)^{\gamma/(\gamma-1)} \tag{11}$$

$$\frac{\rho_0}{\rho} = \left(1 + \frac{\gamma - 1}{2} M^2\right)^{1/(\gamma-1)} \tag{12}$$

The next important equation in nozzle design is the area-Mach number relation (equation 13), which relates the local area ratio and Mach number in the flow. This relation shows that the Mach number at any point in a nozzle is a function of the ratio between the area at that point and the area of the throat. This relationship demonstrates that in order to accelerate a flow past Mach one, the nozzle must diverge. This forms the basis for converging-diverging nozzles in rocket design.

$$\left(\frac{A}{A_t}\right)^2 = \frac{1}{M^2}\left[\frac{2}{\gamma + 1}\left(1 + \frac{\gamma - 1}{2} M^2\right)\right]^{(\gamma+1)/(\gamma-1)} \tag{13}$$

The area-Mach number relationship also gives rise to the condition of choked flow. Since sonic (M=1) flow in the nozzle throat is a prerequisite to achieving a supersonic exit velocity, the conditions in the nozzle throat are determined solely by the stagnation conditions. Noting the assumption of steady flow, the mass flow rate through the nozzle can be written as equation 14 [11].

$$\dot{m} = A_t \frac{P_0}{\sqrt{RT_0}} \sqrt{\gamma \left(\frac{2}{\gamma + 1}\right)^{\frac{\gamma+1}{\gamma-1}}} \tag{14}$$

This mass flow rate equation, coupled with the calculation of exit velocity, gives a means to calculate the thrust produced by an ideal nozzle. In order to find the jet exit velocity, the equation for stagnation pressure can be recast to give Mach number. Then, noting that the speed of sound for an ideal gas is given by equation 15, we find that the jet exit velocity is given by equation 16 [11].

$$a = \sqrt{\gamma RT} \tag{15}$$

$$V_e = \sqrt{\frac{2\gamma}{\gamma - 1} RT_0 \left[1 - \left(\frac{P_e}{P_0}\right)^{\frac{\gamma-1}{\gamma}}\right]} \tag{16}$$

Finally, the predicted thrust is given by combining of the mass flux and exit velocity expressions to arrive at equation 17. This expression represents the design thrust for the nozzle. At this design point, the jet is said to be perfectly expanded, meaning that the exit plane pressure is equal to the ambient pressure.

$$\tau = A_t P_0 \sqrt{\frac{2\gamma^2}{\gamma - 1}\left(\frac{2}{\gamma + 1}\right)^{\frac{\gamma+1}{\gamma-1}}\left[1 - \left(\frac{P_e}{P_0}\right)^{\frac{\gamma-1}{\gamma}}\right]} \tag{17}$$

3.2 Coefficient of Thrust

The coefficient of thrust is a dimensionless parameter that characterizes nozzle performance, and can be used to compare the printed and machined nozzles. It is defined by equation 18. Applying the results from previous sections, we can express the ideal thrust coefficient as equation 19 [13].

$$c_\tau \equiv \frac{\tau}{P_0 A_t} \tag{18}$$

$$C_{\tau,ideal} = \gamma \sqrt{\frac{2}{\gamma-1}\left(\frac{2}{\gamma+1}\right)^{\frac{\gamma+1}{\gamma-1}}\left[1-\left(\frac{P_e}{P_0}\right)^{\frac{\gamma-1}{\gamma}}\right]} + \frac{A_e}{A_t}\left(\frac{P_e}{P_0}-\frac{P_a}{P_0}\right) \quad (19)$$

We then see that ideal thrust coefficient depends solely on the gas specific heat ratio, nozzle area ratio, ambient pressure ratio, and exit pressure ratio. Noting that the exit pressure ratio is a function of nozzle area ratio, we can express this dependence as equation 20. Furthermore, the ideal thrust coefficient does not rely on the stagnation temperature or molecular weight of the gas (equation 21). Although a high temperature propellant offers a greater specific impulse, the propellant temperature has no effect on nozzle performance and thus has no effect on the thrust coefficient. This allows us to use thrust coefficient as a metric for nozzle performance, removing the effects that the test conditions such as temperature may have on the thrust produced.

$$C_{\tau,ideal} = f(\gamma, \frac{A_e}{A_t}, \frac{P_a}{P_0}) \quad (20)$$

$$C_{\tau,ideal} \neq f(T_0, MW) \quad (21)$$

Now that we have developed the analytical tools necessary to analyze nozzle performance, we can apply these principles to the practical design of a cold gas thruster system.

3.3 Propellant Selection

The first step in the design of a cold gas thruster system is the selection of a suitable propellant. Keeping in mind the stringent mass restrictions for spaceflight, the propellant should have a high specific impulse to be considered for this application. Specific impulse is a measure of the impulse delivered by a propellant per unit weight, and is related to thrust by equation 22.

$$I_{sp} = \frac{\tau}{g_0 \dot{m}} \quad (22)$$

Referring back to equation 9 for thrust, we find that the specific impulse can be rewritten as equation 23.

$$I_{sp} = \frac{1}{g_0 \dot{m}}[\dot{m}V_e + (P_e - P_a)A_e] \quad (23)$$

Finally, we can consider the case of a perfectly expanded jet ($P_e = P_a$), where nozzle performance is maximized. In this case, the pressure component of thrust is zero, and only the momentum component remains. Considering the case of perfect expansion and substituting equation 16 for jet exit velocity, we find that the ideal specific impulse can be expressed as equation 24.

$$I_{sp} = \frac{1}{g_0}\sqrt{\frac{2\gamma}{\gamma-1}RT_0\left[1-\left(\frac{P_e}{P_0}\right)^{\frac{\gamma-1}{\gamma}}\right]} \quad (24)$$

From this expression it can be clearly seen that stagnation temperature and pressure directly affect the specific impulse. This explains why hot burning, high pressure bipropellant engines are among the most efficient chemical rockets. In the case of cold gas thrusters, however, the stagnation temperature of the propellant is not controlled, but rather assumes the temperature of the surrounding spacecraft or environment. A less obvious result of equation 24, however, is the dependence of specific impulse on gas properties γ and R. Noting that the ideal gas constant is related to the universal gas constant through

equation 25, one can see that the ideal specific impulse is also influenced by the molecular weight of the propellant, with lighter molecules yielding a higher specific impulse.

$$R = \frac{R_u}{MW} \tag{25}$$

In order to better understand the impact of operating pressure and propellant selection, the ideal specific impulse is plotted in figure 10 for various propellants under consideration. This plot was generated by assuming a stagnation temperature of 300K and constant specific heat ratios. The dependence of specific impulse on molecular weight is clearly reflected in the plot, with lighter molecules showing higher specific impulses regardless of pressure ratio.

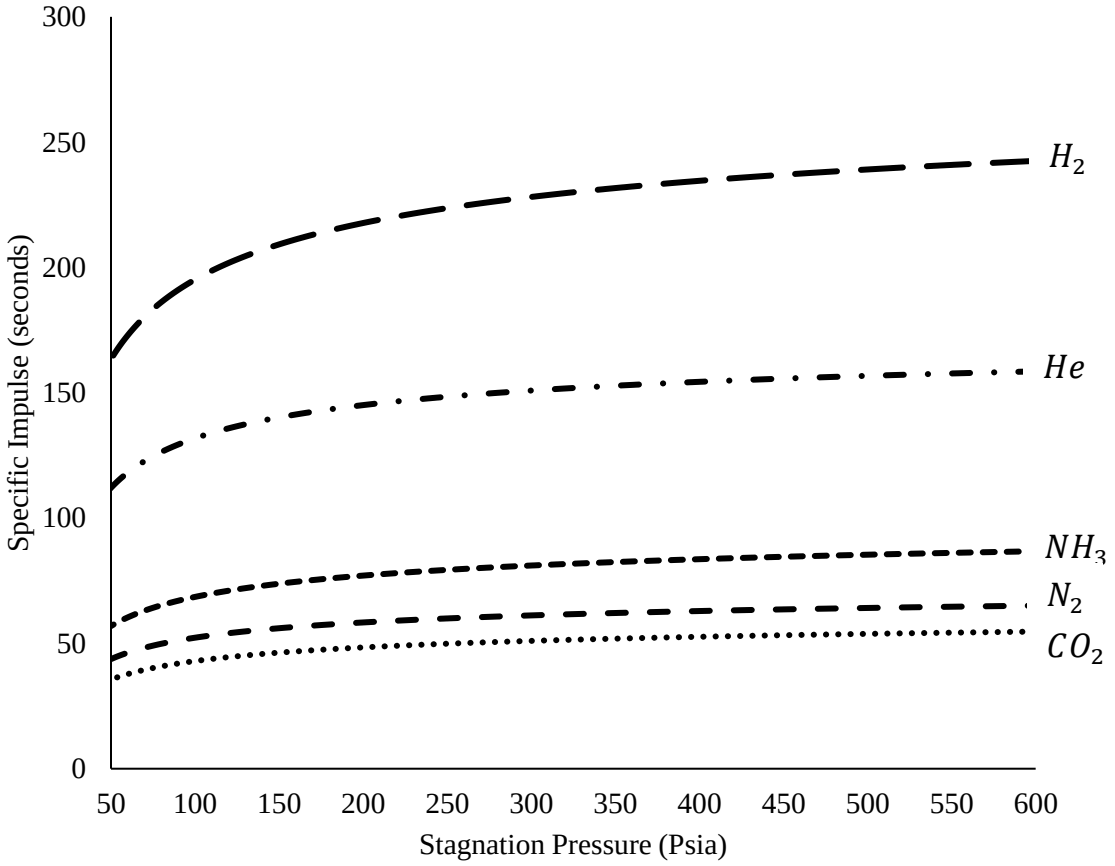

Figure 10: Stagnation pressure vs. specific impulse for various Cold Gas propellants

Another important factor to consider in propellant selection is storage volume for the fuel, as excessive tank volume can raise the weight of the overall system and offset the high specific impulse of a given propellant. To take this effect into account, table 1 summarizes the propellant densities at 3,000 Psi. Although Hydrogen and Helium have substantially higher specific impulse than the other propellants, their low density requires prohibitively large tanks for storage. Furthermore, Hydrogen gas poses serious safety risks for the spacecraft and personnel during system development and testing. Nitrogen, a commonly used propellant for cold gas thrusters, shows a good combination of density and specific impulse, and is an inert gas. Ammonia and carbon dioxide both store as liquids at this pressure, leading to very high storage densities. Although in some applications this may be desirable, it adds to the system

complexity, requiring a chamber prior to the nozzle for the liquid to fully evaporate. Further, based on ambient temperature there could be evaporation and associated pressure rise, requiring venting capability.

Propellant	Density (g/cc)	Ideal Specific Impulse (s)
Hydrogen	0.02	237
Helium	0.04	156
Nitrogen	0.26	64
Ammonia	Liquid	85
Carbon Dioxide	Liquid	53
Oxygen	0.28	59

Table 1: Propellant density at 3,000 Psi and specific impulse at 450 Psi

For this study, nitrogen gas offers the best combination of properties and cost. There is, however, the additional concern of asphyxiation associated with using pure Nitrogen as a propellant. The human body detects suffocation by the buildup of carbon dioxide, rather than the lack of oxygen. This presents a hazard to personnel working on the system, and can potentially lead to lethal asphyxiation without proper warning. For this reason, it was decided to use a 50/50 blend of nitrogen and breathing grade air as a propellant. This modification does not significantly impact the performance or storage volume of the propellant while eliminating the risk of asphyxiation.

3.4 Selection of Operating Pressure

Now that a suitable propellant has been selected for the cold gas thruster, an operating pressure must be chosen for the nozzle stagnation chamber. Cold gas thruster systems for spaceflight typically use operating pressures on the order of 120 psi [14]. Although a higher specific impulse can be realized using higher operating pressures, the gains are offset by the higher weight of components that must withstand this pressure. For the present study, it is of interest to evaluate the RPT nozzles for structural durability, thus the operating pressure should be higher than is typical for Spaceflight.

A physical limit on operating pressure can be determined by considering the thermodynamic state of the gas throughout the nozzle. If the gas drops below the boiling point at any point in the system, it will begin to condense and form a two phase flow, invalidating the performance predictions from the previous sections. To evaluate the potential for this, we can consider the conditions at the nozzle exit, as it is the coldest point in the system. Table 2 shows the boiling points for each constituent species in the propellant gas at the design exit pressure of one atmosphere.

Gas	% by Volume	% by Weight	Boiling Point at 1 atm (K)
Nitrogen	89.04	87.73	77.4
Oxygen	10.48	11.60	90.2
Argon	0.46	0.64	87.3
Carbon Dioxide	0.02	0.03	194.7

Table 2: Major species in propellant and associated boiling points

The highest boiling point of any gas species in the propellant is that of carbon dioxide, at 194.7 K. In order to maintain the nozzle exit temperature above this value, the stagnation pressure would need to be maintained below 65 Psi. At this pressure, the specific impulse is substantially below the maximum value and the structural integrity of the RPT nozzle cannot be evaluated. Since carbon dioxide accounts for only 0.03% of the propellant by weight, allowing the exit temperature to drop below the species boiling point will not significantly impact thruster performance. The next highest species boiling point is that of oxygen at 90.2 K. Since oxygen represents 11.6% of the propellant mass, it is important that the propellant exit temperature be maintained above this value. The maximum stagnation pressure that can be used based on this restriction is approximately 950 Psi.

The restriction imposed by the boiling point of oxygen ($P_0 < 950\ Psi$) is nearly an order of magnitude higher than those typically used for in-Space applications [14]. Because of this, an intermediate stagnation pressure of 450 Psi was selected to achieve a good specific impulse and to not impose unnecessarily strict requirements on the pressure regulator hardware. By using this intermediate stagnation pressure, the propellant pressure regulator may be easily sourced from commercial off the shelf components.

3.5 Selection of Nozzle Dimensions

The nozzle operating conditions established in previous sections are summarized in table 3. Using these operating conditions, we can apply the analytical framework established in section 3.1 to the design of an appropriate nozzle.

Operating Parameter	Value
Stagnation Pressure	450 Psi
Stagnation Temperature	300 K
Exit Pressure	14.7 Psi
Propellant	50/50 Air/Nitrogen blend

Table 3: Cold Gas thruster operating conditions

To begin, we can rewrite equation 11 to solve for Mach number from the given pressure ratio. Once the exit Mach number is known, it can be used to calculate the exit temperature (equation 27) and sound speed (equation 28). Then, the jet exit velocity can be calculated from the exit Mach number and sound speed (equation 29). We can then solve for the exit area ratio by an iterative solution to the area-Mach

number relation (equation 13), and find the appropriate exit area ratio to achieve the desired exit Mach number.

$$M_e = \sqrt{\frac{2}{\gamma - 1}\left[\left(\frac{P_0}{P_e}\right)^{\frac{\gamma-1}{\gamma}} - 1\right]} = 2.88 \tag{26}$$

$$T_e = T_0\left[1 + \frac{\gamma - 1}{2}M_e^2\right]^{-1} = 113\ K \tag{27}$$

$$a_e = \sqrt{\gamma R T_e} = 217\ m/s \tag{28}$$

$$V_e = M_e a_e = 624\ m/s \tag{29}$$

$$\frac{A_e}{A_t} = 3.78 \tag{30}$$

At this point, we can again consider the objectives of this study, namely to pick sufficiently small nozzle dimensions to test the manufacturing resolution and quality of the RPT nozzles, while still maintaining the ability to machine a conventional nozzle to serve as a reference for comparing nozzle performance. After consulting the resident machinist at Vanderbilt University, a throat diameter of 1.5 mm was selected as the smallest diameter that could be easily machined. Applying this throat diameter, we can then calculate the appropriate exit diameter.

$$d_t = 1.5\ mm$$

$$\frac{d_e}{d_t} = \sqrt{\frac{A_e}{A_t}} \tag{31}$$

$$d_e = d_t\sqrt{\frac{A_e}{A_t}} = 2.91\ mm \tag{32}$$

In order to supply adequate airflow to the nozzle, the diameter of piping upstream of the nozzle must be properly sized. A criteria was established that states the pipe area upstream of the nozzle should be at least four times the diameter as the nozzle throat, corresponding to a cross sectional area that is sixteen times larger than the nozzle throat. This requirement yields an upstream diameter of 6 mm, and an upstream pipe size of 0.25" (6.25 mm) was chosen.

3.6 Selection of Nozzle Geometry

Now that the nozzle dimensions have been determined, an appropriate geometry must be selected as well. In the case of the machined nozzles, the shape of the nozzle must be selected so that it can be fabricated by conventional methods. This implies that a simple conical nozzle is needed, with constant angles of convergence and divergence. A converging half angle of thirty degrees was chosen after a brief survey of the literature. In the case of the diverging angle, a lower diverging angle produces an exit velocity that is more axial than a high divergence angle, but also contributes to a longer nozzle and more viscous losses due to increased travel distance along the nozzle walls. To balance these considerations, and to provide an angle for which tooling was readily available, a diverging half angle of ten degrees was chosen.

The geometry of the RPT and machined nozzles are shown in figures 11 and 12. The most notable difference between the two geometries is the presence of sharp corners in the machined nozzle. These corners result from the method used to machine the nozzle, and cannot be easily smoothed. This issue underscores the benefits of additive manufacturing in fabricating nozzles with small dimensions. Although the analytical equations predict the same thrust from each nozzle, the corners present in the machined nozzle are likely to result in the formation of shock waves in the flow, causing deviations from isentropic flow and reducing performance.

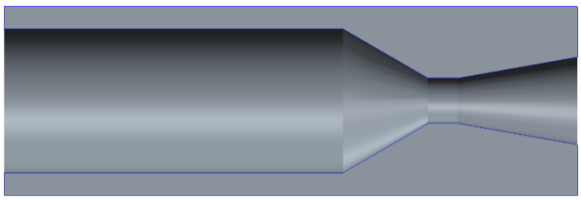

Figure 11: Machined nozzle geometry

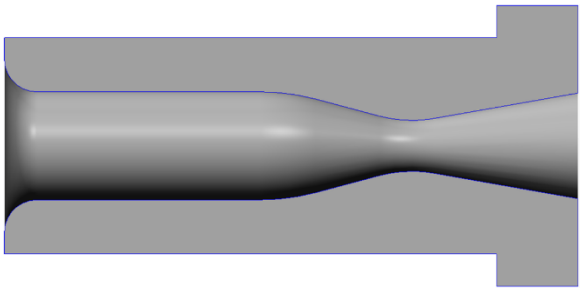

Figure 12: RPT nozzle geometry

The throat region of the printed nozzle was designed using criteria established for large nozzles, which states that the radius of curvature in the nozzle throat should be at least two times the throat radius in order for one-dimensional flow theory to remain valid [15]. The radius of curvature was chosen to be five times the throat radius in order to prevent imperfections during printing from resulting in a radius of curvature below this value.

While the geometry of the machined nozzle is well known from the machining techniques and tooling used, the RPT nozzle geometry is subject to defects or errors that can result from the printing process. In order to assess the quality of the printed nozzle, and to check for the presence of such defects, the nozzle geometry was visually inspected after printing was completed (figure 13). The RPT nozzle appears to be a close match of the design (figure 14), showing no visible defects or sharp edges. Note that the RPT nozzle was placed in a shallow bath of water to increase the transparency of the nozzle material.

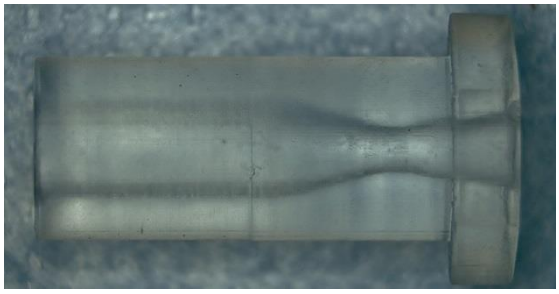

Figure 13: RPT nozzle as printed

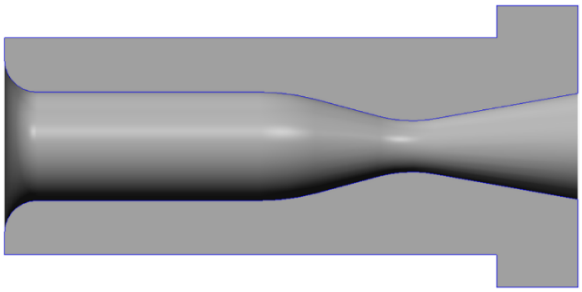

Figure 14: RPT nozzle geometry

3.7 System Integration

Once the nozzles were designed and the dimensions known, it was necessary to select the other hardware needed to deliver gas to the nozzles for testing. These major components include a tank to hold the pressurized gas, a pressure regulator, a solenoid valve, and the necessary fittings and tubing to connect the components. Note that the components used for testing differ slightly from those used in the 2016-17 Student Launch project in order to allow for easy integration with the thrust stand, and accommodation of the pressure transducer. A schematic overview of the test system is shown in figure 15 below.

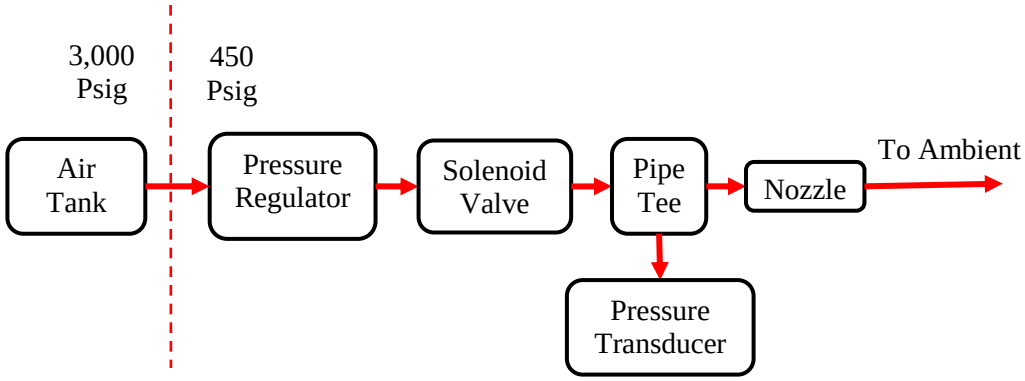

Figure 15: Propellant flow diagram

The first component that was selected after sizing the nozzles was the air tank. A small air tank was selected so that integration with the thrust stand would be simplified. The air tank and pressure regulator were sourced from the recreational paintball market due to the availability, low cost, and safety certifications carried by these parts. The air tank chosen is a 13 cubic inch aluminum tank sold by Ninja paintball. The air tank is rated to pressures up to 3,000 psi and was matched with a pressure regulator manufactured by Custom Products. This tank regulator steps the delivery pressure from 3,000 psi down to a nominal pressure of 450 psi. The regulator also incorporates burst discs to protect both the high pressure (5K psi) and low pressure (1.8K psi) sides of the regulator.

The next component in the gas delivery system is the solenoid valve, which opens to allow the thruster to be fired. The solenoid valve has unusually strict design requirements, both operating at a high pressure of up to 600 psi and needing a relatively large orifice to supply air to the nozzle. It is particularly important that the solenoid orifice is larger than the nozzle throat to prevent choking in the solenoid valve, and a larger throat is desirable to minimize the pressure loss across the solenoid valve and maximize the nozzle stagnation pressure. After consulting the solenoid valve catalog from Parker Hannifin, a pilot operated solenoid valve was selected. The valve has a maximum operating pressure of 1,500 psi and an orifice size of 0.25”, significantly above the nozzle throat diameter.

Finally, steel tubing with a pressure rating of 5,000 psi was used to connect the pressurized components in the gas delivery system. Swagelok connectors were used with the tubing to provide a high pressure seal and minimize the risk of metal shavings or other debris from blocking the valve or nozzle. This system was assembled and integrated into a custom built thrust stand for precision thrust and pressure measurements of the nozzles to be tested. The design and details of this thrust stand are covered in detail in the next section.

3.8 Thrust Stand Design

The thrust stand used in this study was designed and built specifically for cold gas thrusters producing up to 15 Newtons of thrust. A schematic of the thrust stand is shown in figure 16. Pressure and thrust are simultaneously measured as the thruster is fired. The load cell is placed horizontally with respect to the nozzle to remove the effect of gravity from thrust measurements. The pressure transducer is located directly upstream of the nozzle, connected with large diameter piping over a distance of approximately ½” to minimize the thrust loss between the transducer and the nozzle. Rigid piping is used throughout the system to reduce vibration associated with flexible hoses and to remove the bias typically introduced by propellant lines. The thruster and air tank are constrained on a moving platform, which allows thrust to be translated to the load cell without requiring the tubing to bend.

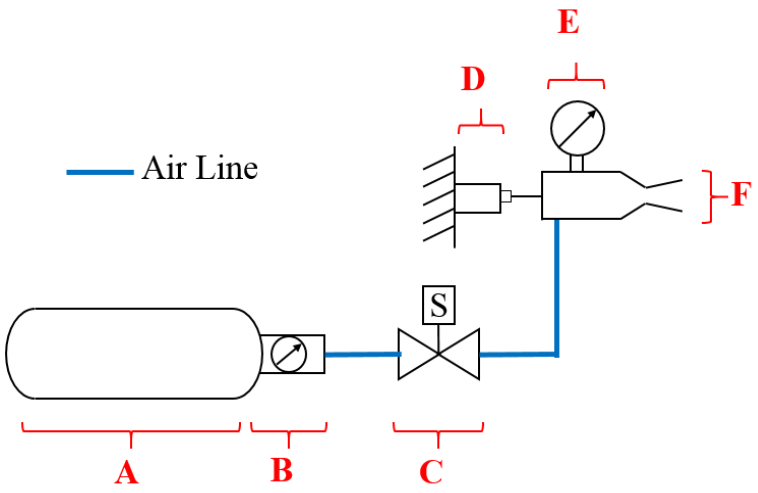

Figure 16: Thrust Stand Schematic- (A) Air Tank, (B) Pressure Regulator, (C) Solenoid Valve, (D) Load Cell, (E) Pressure Transducer, (F) Nozzle.

The physical implementation of the VADL thrust stand is shown in figure 17. The thrust stand design is loosely based on the design presented in [10], with the notable difference of removing the bias introduced by using an external propellant feed line. The air tank, pressure regulator, and feed line are mounted on a moving platform along with the control solenoid valve and nozzle. This platform is suspended by two thin steel plates that allow platform to move axially but constrain it in both perpendicular directions. The platform is directly attached to a load cell, which measures the thrust produced when the thruster is operated. The supporting structure for the stand is bolted to a vibration isolating optical table in order to mitigate the effects of external vibrations. A pulse generator and power supply were used to trigger the solenoid valve for testing, and thrust and pressure data were recorded using a National Instruments 6212 data acquisition system and LabVIEW software.

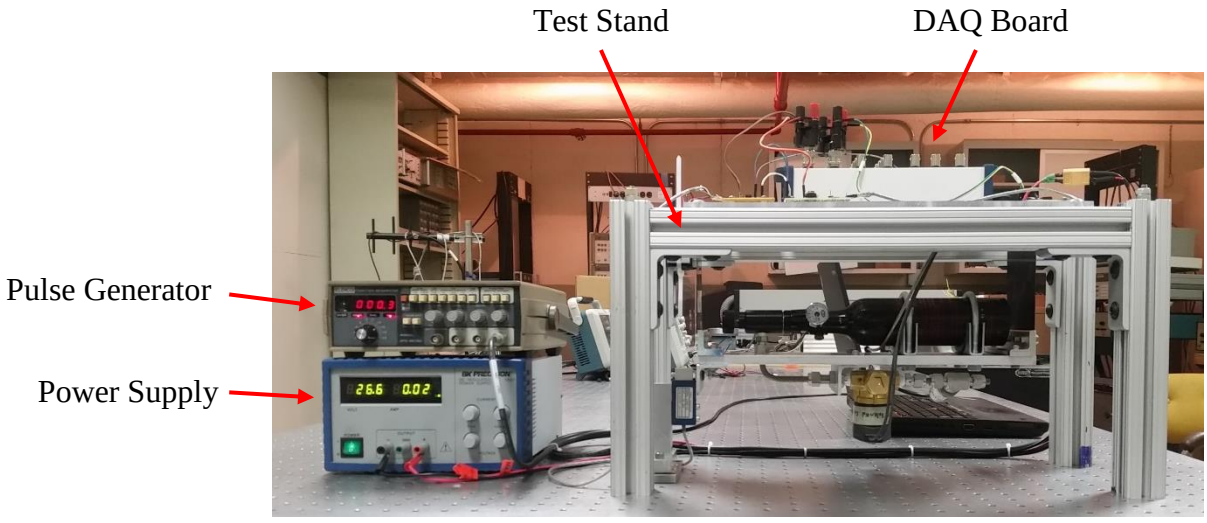

Figure 17: Thrust stand arrangement showing structure, data acquisition system, pulse generator and power supply

The hardware necessary to deliver the cold gas propellant is mounted directly on the moving platform along with the nozzle. A section or rigid steel tubing carries the gas from the pressure regulator to the

solenoid valve. The output of the solenoid valve is connected to a pressure transducer and to the nozzle. Unlike most thrust stands, there is no bias introduced by using external feed lines for the propellant. These biases can be particularly difficult to mitigate because the rigidity and load imposed by the feed line varies with line pressure. Since delivery pressure changes over the course of the experiment, the bias introduced by an external feed line cannot simply be removed during calibration, and can negatively impact the precision and experimental uncertainty.

Gas is stored in the tank at 3,000 psi and regulated down to 450 psi by the attached pressure regulator. The 450 psi gas is then delivered through steel tubing with Swagelok connections to the solenoid valve. When triggered, the solenoid valve opens and delivers air to the nozzle through a tee connector. This connector serves both as a reservoir for the nozzle, and allows a pressure transducer to directly measure the nozzle plenum pressure. The thrust stand is designed to operate in ambient conditions rather than in a vacuum chamber to reduce the cost and complexity of the system.

Figure 18 shows a close up of the load cell and connection to the moving platform. The load cell is directly bolted to the moving platform using a steel bolt and locknuts to prevent loosening of the connection due to vibration. Two O-rings are placed on either side of the bracket connecting bracket to provide vibration damping for the system. The load cell is mounted on a rigid support that is bolted to the optical table. This mounting arrangement prevents thrust loads from being transferred to the test stand support structure, which is considerably less rigid and more prone to vibration.

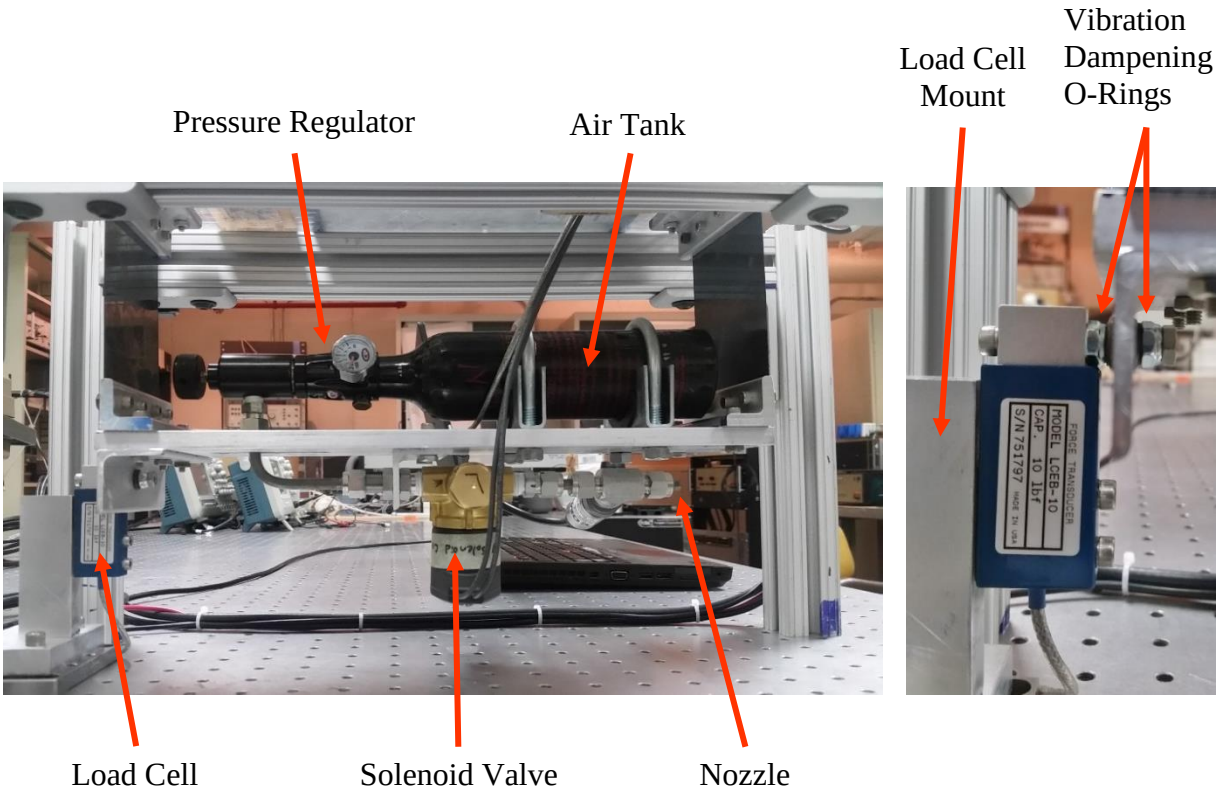

Figure 18: (Left) Thrust stand moving platform (Left) and Load cell and mount (Right)

CHAPTER 4

MEASUREMENT AND INSTRUMENTATION

Thrust and pressure data were recorded using a National Instruments NI 6212 Data Acquisition board. Custom analog circuitry was designed to condition and amplify instrumentation signals prior to being read by the DAQ board, and the collected data was post-processed digitally for data reduction. The details of the instrumentation systems and data collection are covered in this section. For a detailed description of the analog instrumentation circuitry, refer to Appendix A.

4.1 Thrust Measurement

Thrust measurements were taken using an Omega LCEB-10 load cell (figure 19), which has a capacity of 44 N and a millivolt output (table 4). The load cell was selected for its excellent accuracy, hysteresis, and repeatability. The load cell is based on a full Wheatstone bridge configuration of strain gauges, and measures both compressive and tensile loads.

Figure 19: Omega LCEB-10 load cell

Capacity	44 N (10 lbf)
Excitation	10 V
Output	3 mV/V
Linearity	$\pm$0.03% FS
Hysteresis	+-0.02% FS
Repeatability	+-0.01% FS
Thermal Shift	$\pm 8\ ppm/°F$ FS

Table 4: Load cell specifications

In order to improve the precision and resolution of measurement, the millivolt signal produced by the load cell must be conditioned and amplified before being read by the DAQ board. Figure 20 shows the signal path starting at the load cell. The analog signal is carried by a shielded pair of wires to an analog circuit. This circuit first applies a 3 kHz low pass filter to remove the noise introduced due to electromagnetic interference from the environment, which appears as a common mode voltage on the signal lines. The signal is biased slightly due to the pretensioning of the load cell. This bias is removed and second set of low pass filters are applied before the signal is amplified to match the -5V to +5V input range of the analog to digital converter (ADC) on the DAQ board. The amplified analog signal is then converted to a digital signal by the ADC and is recorded at a sampling rate of 5 kHz. In post-processing, the data is further conditioned by digital bandstop and low pass filters. The bandstop filter reduces noise due to the vibrational response of the thrust stand, which occurs in a narrow band around 48 Hz. For an in-depth analysis of the thrust stand bandwidth and vibrational response, refer to Appendix B. An average value of the filtered signal is then taken to determine the average thrust value for the sample.

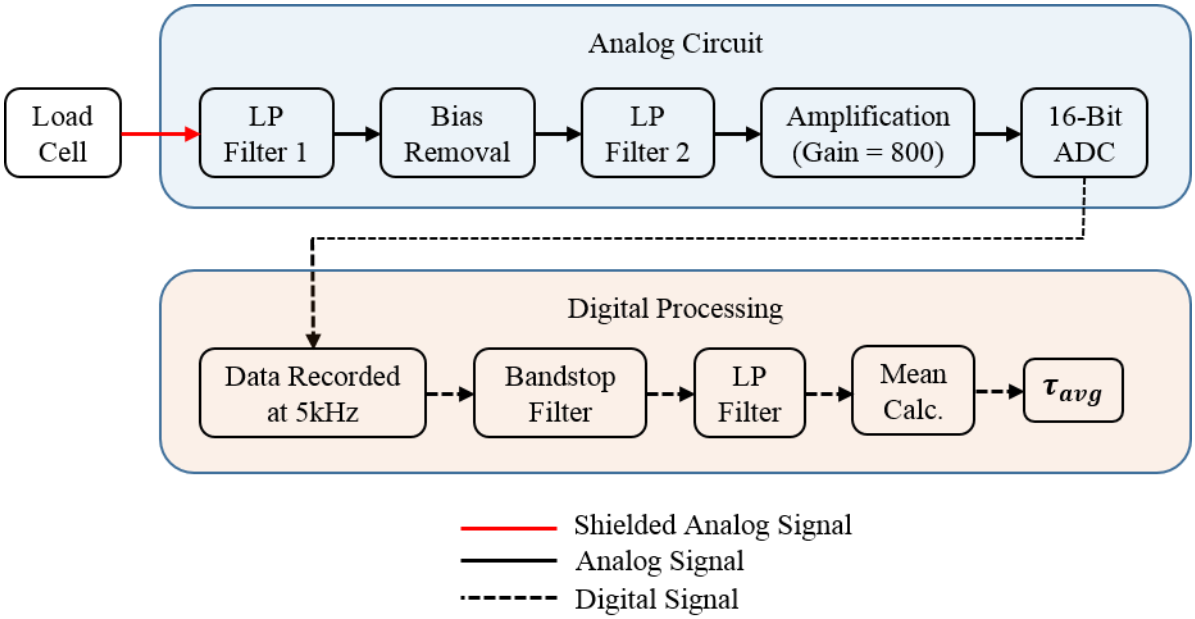

Figure 20: Flow diagram for thrust data acquisition, signal conditioning, and data reduction

In order to determine the appropriate calibration factor for the amplified load cell signal, a calibration test was conducted. A known load was applied directly to the nozzle using an Extech 475044 digital force gauge while the amplified signal was recorded by the DAQ board. Loads of 5N, 10N, and 15N were applied three times each, returning to zero load between each measured point. This procedure gave a total of nine data points, which are plotted in figure 21. The calibration curve lies within the specified accuracy of the Extech digital force gauge, indicating that the limiting factor in the accuracy of the calibration is the Extech force gauge rather than the load cell or measurement circuitry. This procedure also allowed the zero to be measured multiple times, and the measured zero shifted less than 10 mV during calibration.

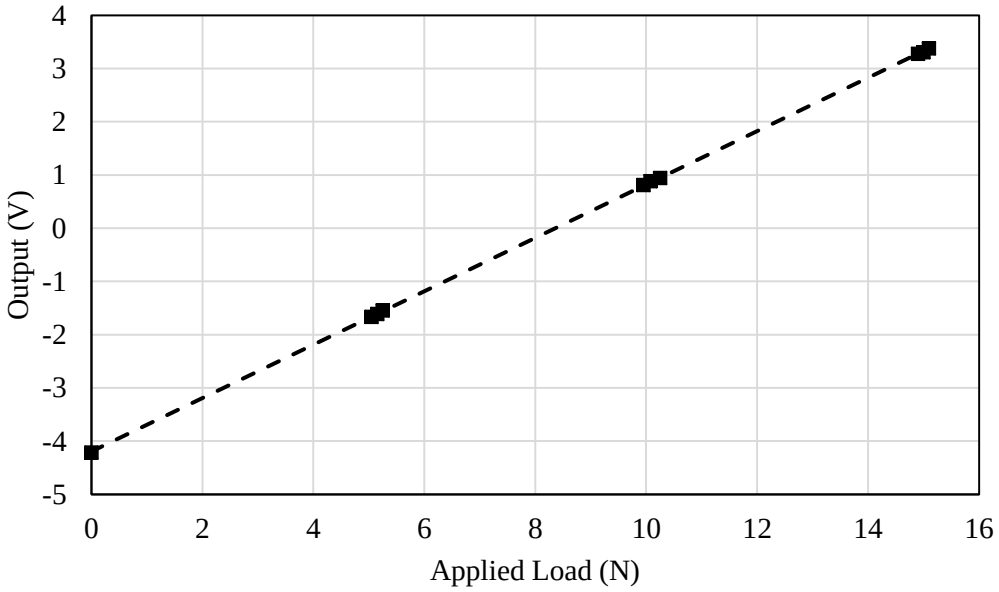

Figure 21: Calibration curve for thrust measurement

4.2 Pressure Measurement

The nozzle plenum pressure was measured using an Omega PX309 pressure transducer (figure 22). This transducer has an input pressure range of 0-1,000 Psig and outputs a signal from 0-100 mV. This transducer was selected for its high accuracy and fast response time (table 5). In order to accurately measure the pressure in the nozzle plenum, the pressure transducer is placed on a tee connection immediately before the nozzle. This placement ensures that the pressure drop between the pressure transducer and the nozzle inlet is negligible.

Figure 22: Omega PX309 pressure transducer

Input Range	0 – 1,000 Psig
Excitation	5 V
Output	20 mV/V
Accuracy	±0.25% BSL
Response Time	<1 ms
Bandwidth	DC to 1kHz

Table 5: Pressure transducer specifications

The signal path for pressure measurement (figure 23) is similar to that of the load cell, but is notably simpler. The pressure data has only a small bias compared to the output range of the transducer, eliminating the need for a bias removal stage. The analog signal is carried from the pressure transducer through a shielded pair of wires to the analog circuitry. A 3 kHz low pass filter removes common mode noise from the signal and a differential low pass filter limits signal noise above 160 Hz. The signal is then amplified and read by the 16 bit ADC. Data is recorded at 5 kHz and the mean is calculated in post processing to determine the average pressure.

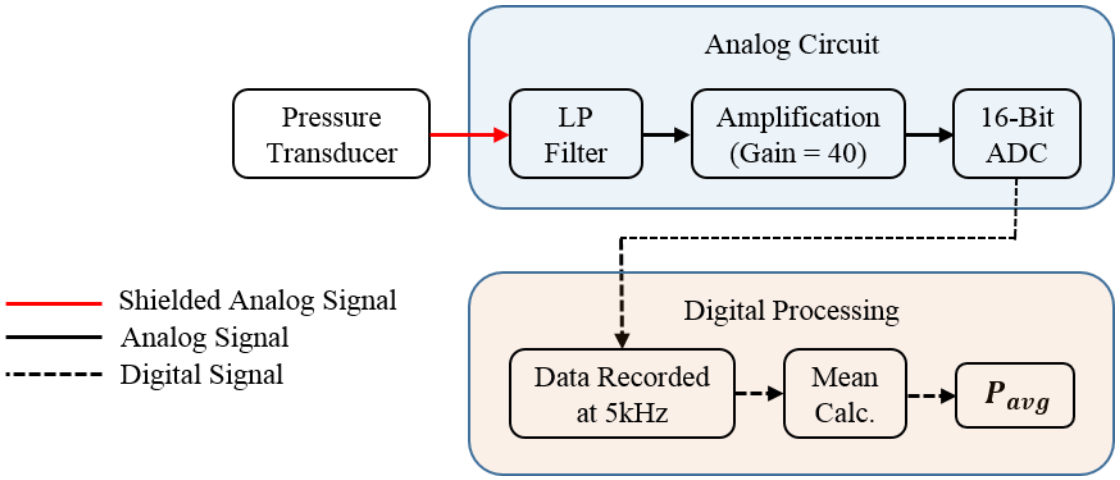

Figure 23: Flow diagram for pressure data acquisition, signal conditioning, and data reduction

Since the pressure transducer is placed perpendicular to the flow, the measured pressure in the tee connector is the static, rather than stagnation pressure. Since the stagnation pressure is of more use in nozzle performance analysis, this static pressure measurement must be converted into the stagnation pressure using the area ratio between the upstream pipe and the nozzle throat. Based on the Mach-area relationship, the Mach number at the point of pressure measurement is 0.14, and the static pressure at this point is 98.6% of the stagnation pressure. This pressure measurement is corrected according to this calculation in the data presented in section 5.

CHAPTER 5

RESULTS

In order to evaluate the performance of rapid prototyped nozzles compared to machined nozzles, a series of thrust tests were conducted using the VADL thrust stand. Two pairs of nozzles were tested, one rapid prototyped pair and one machined pair. The pairs were identical copies of each other in order to provide a means of evaluating the repeatability of the tests. In order to mitigate thermal effects, it was decided to pulse the thrusters during testing. The average thrust and pressure recorded during each pulse would be interpreted as a single data point and used for the performance comparison. For each test, the air tank was filled to a pressure of 3,000 psig and a pulse generator was used to control the solenoid. A pulse duration of 0.25 seconds was used with approximately 3.5 seconds between pulses.

In this section, the raw data will be presented and the data reduction techniques will be discussed in detail. The final results will be presented in terms of the coefficient of thrust and will be used to compare the performance of the rapid prototyped and machined nozzles.

5.1 Raw Data

The raw data for a representative pulse of a rapid prototyped nozzle is shown in figure 24. The thrust data is 'raw' in the sense that the digital bandpass and low pass filters shown in figure 20 have not yet been applied. Both signals have been conditioned and amplified by analog circuitry and recorded at 5 kHz. The large fluctuations in the thrust data ($\pm 3N$) are a result of the vibrational response of the thrust stand when subjected to the sudden increase in thrust. The great majority of the vibrational response occurs at the resonant frequency of the thrust stand, which is discussed further in Appendix B. Another clue that the thrust data indicates a vibration of the thrust stand rather than real thrust fluctuations is that the fluctuations are not seen in the pressure data. Since momentum thrust scales linearly with pressure, one would expect to see large fluctuations in the pressure data if the thrust was truly changing. It is also worth noting that there is a small (~10 psi) hysteresis in the pressure measurement, most likely due to temperature effects not seen during static pressure calibration.

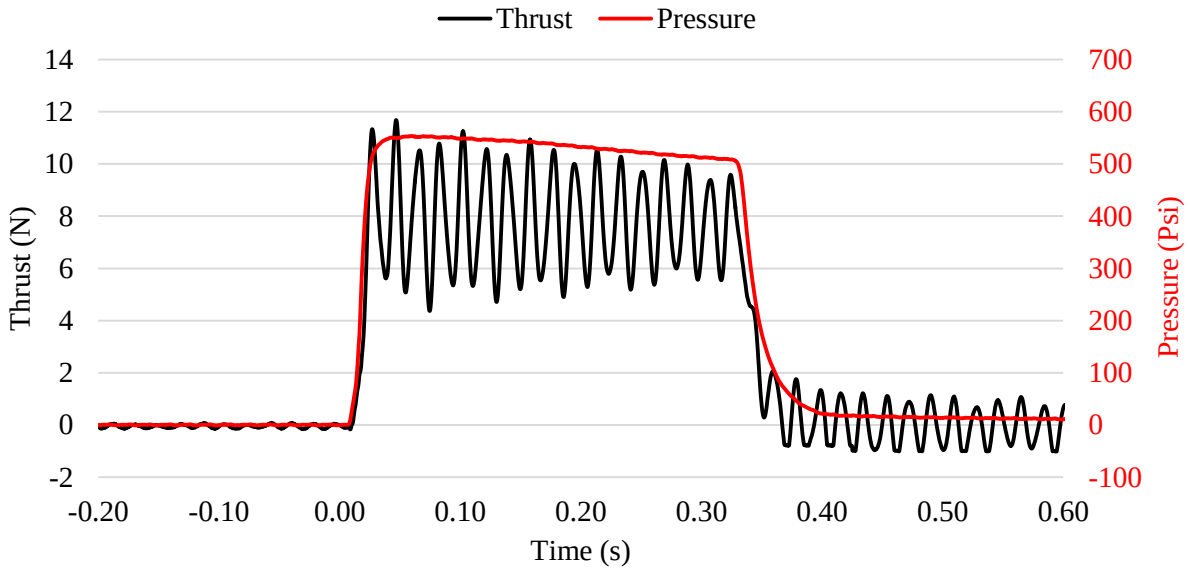

Figure 24: Raw thrust and pressure data for 0.25 second pulse

5.2 Data Reduction

In order to separate the effects of the thrust stand vibrational response from the actual thrust level, digital bandstop and low pass filters were applied to the thrust data. A bandstop, or notch, filter removes vibrations within a narrow band of frequencies from the overall signal. The bandstop filter was designed to attenuate vibrations occurring near the resonant frequency ($48 \pm 5\ Hz$). The low pass filter is then applied with a cutoff frequency of 43 Hz to further smooth the signal within the useful bandwidth. The result of this filtering process can be seen in figure 25. Note that digital filtering is applied to the thrust data but not the pressure data since there is no vibrational noise in the pressure data.

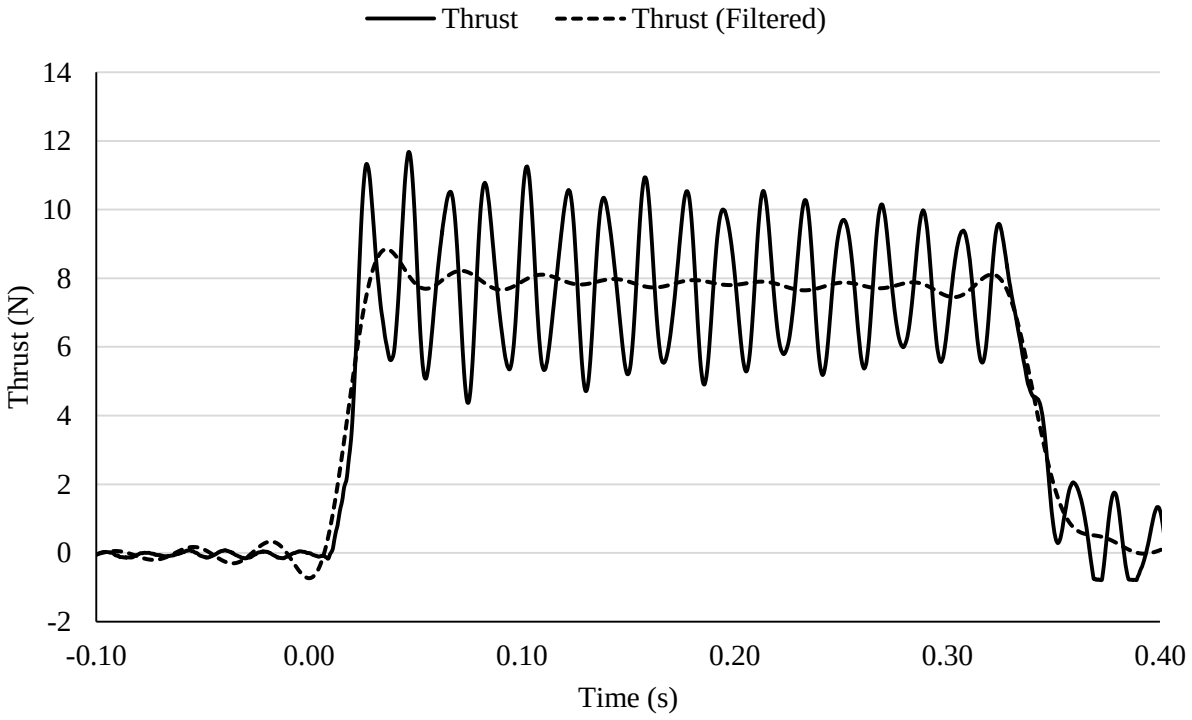

Figure 25: Raw and filtered thrust data for 0.25 second pulse

From figure 25 we can see that the oscillating component of the thrust data has been greatly mitigated through digital filtering. Despite this, the data near the rising and falling edge of the pulse still shows large amplitude oscillations. These oscillations near the pulse edges is an artifact of the digital filtering, which cannot function properly near a sharp rising or falling edge. The filters also cause a small amount of diffusion of the oscillation, which is apparent from the increased fluctuation of the signal immediately before the rising edge of the pulse. Because of this, thrust data away from the rising and falling pulse edges is the most reliable, and the mean thrust value excludes the thrust values near these edges. Figure 26 shows the data used to compute the mean thrust value, which excludes approximately 60 ms (18%) of the data near each pulse edge. The average thrust is calculated from the simple arithmetic mean, which is equivalent to the total impulse divided by the pulse time. The mean pressure is also calculated using the same time interval in order to maintain parity between the mean thrust and mean pressure values.

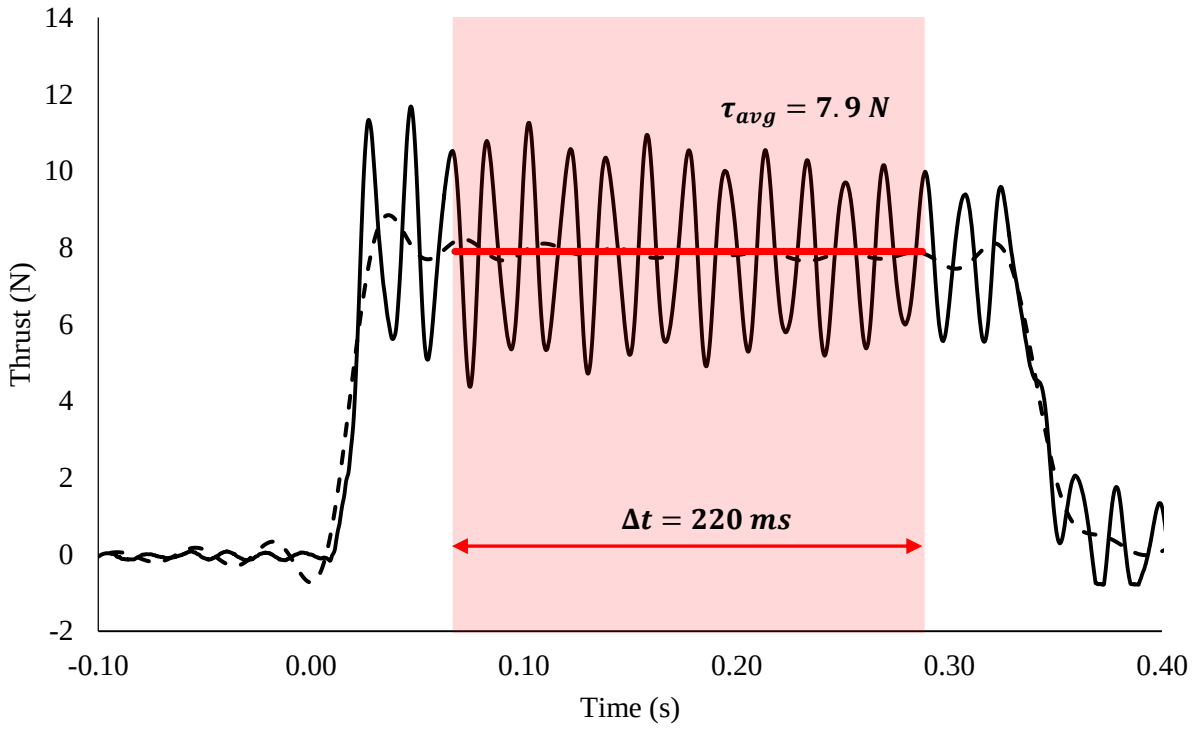

Figure 26: Average thrust for 0.25 second pulse, filtered thrust data was sampled within the red area to obtain the average thrust value

Once the mean thrust and mean pressure values have been calculated, the experimental coefficient of thrust is obtained simply by substituting these values into equation 18 to obtain equation 33.

$$c_\tau = \frac{\tau_{avg}}{P_{0,avg}\, A_t} \tag{33}$$

5.3 Coefficient of Thrust Results

A total of twelve tests were completed to investigate the performance of the printed and machined nozzles. A pair of 'identical' RPT nozzles were tested independently. These nozzles were produced in the same print batch, using the same geometry, settings, and print orientation. A pair of machined nozzles were also tested that were identical within machining and measurement tolerances. Each of the four nozzles were tested three times, using the same test conditions and pulse length for each. The results of these tests have been plotted in figure 27. For each test, there were approximately 8 thruster pulses, and the average thrust and pressure for each pulse was used to generate a single data point. The different symbols used in figure 27 (square, circle, and triangle) denote different tests for a given nozzle. Also shown is the coefficient of thrust predicted by the isentropic flow equations used to design the nozzles.

The clear implication of figure 27 is that the printed nozzles achieved a substantially higher coefficient of thrust than the machined nozzles over the whole range of stagnation pressures. At the design point of 450 psia, the coefficient of thrust for the printed nozzles is approximately 8% lower than ideal, while the machined nozzles' was approximately 12% lower. Although the scatter in the data in figure 27 is low, the measurement uncertainty must be evaluated in order to assess the confidence of this conclusion. The next

section will focus on identifying the contributions to measurement uncertainty and quantifying the overall uncertainty in the coefficient of thrust measurements.

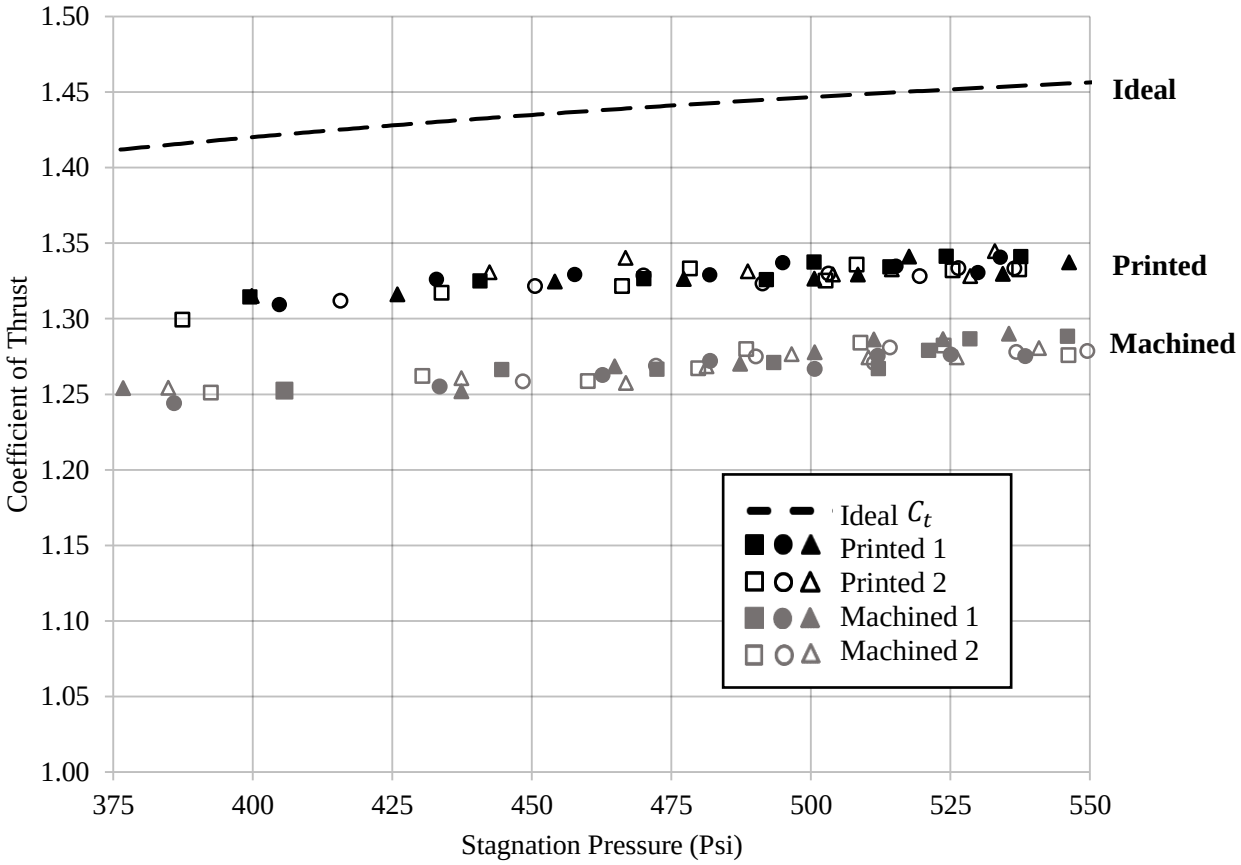

Figure 27: Experimental coefficient of thrust for RPT and machined nozzles

CHAPTER 6

DISCUSSION

6.1 Uncertainty Analysis

In order to quantify the uncertainty in coefficient of thrust, the underlying contributions must be identified and used to calculate the overall measurement uncertainty. This analysis will initially be separated in the three terms seen on the right hand side of equation 33- thrust, pressure, and throat area. The resulting uncertainty for each of these terms will then be combined to find the uncertainty in coefficient of thrust, as shown in equation 34 below.

$$\frac{\Delta C_\tau}{C_\tau} = \sqrt{\left(\frac{\Delta \tau}{\tau}\right)^2 + \left(\frac{\Delta P_0}{P_0}\right)^2 + \left(\frac{\Delta A_t}{A_t}\right)^2} \tag{34}$$

6.1.1 Uncertainty in Thrust Measurement

The uncertainty in thrust can be estimated from the calibration technique and associated calibration curve (figure 21). The overall contributions to uncertainty in thrust measurement include the uncertainty in the force applied during calibration, and the uncertainty in measurement of the amplified load cell signal. The uncertainty in thrust can then be expressed by equation 35.

$$\frac{\Delta \tau}{\tau} = \sqrt{\left(\frac{\Delta F}{F}\right)^2 + \left(\frac{\Delta v_\tau}{v_\tau}\right)^2} \tag{35}$$

Since all points on the calibration curve lie within the specified accuracy of the Extech digital force gauge used for calibration, we can use the uncertainty in applied force to represent the contributions of both the load cell and the force gauge. This gives an uncertainty in applied force of a constant 0.05 N. The uncertainty in measured voltage is $\pm 1.42\ mV$ based on the manufacturer's specifications for the DAQ board analog to digital converter. Finally, these values can be combined to find the uncertainty in measured thrust (equation 38). Rather than being a fixed value or percent, the fractional uncertainty in thrust depends on the magnitude of the thrust, and thus will vary for each data point.

$$\Delta F = \pm 0.05\ N \tag{36}$$

$$\Delta v = \pm 1.42\ mV \tag{37}$$

$$\frac{\Delta \tau}{\tau} = \sqrt{\left(\frac{0.05N}{F}\right)^2 + \left(\frac{1.42mV}{v_\tau}\right)^2} \tag{38}$$

6.1.2 Uncertainty in Pressure Measurement

The uncertainty in pressure measurement was obtained from a NIST traceable manufacturer calibration performed by Omega Engineering. The certification paperwork delivered with the pressure transducer indicates an accuracy of 0.25% (0.0025) of the measured pressure throughout the rated pressure range. The uncertainty in measured voltage also contributes to uncertainty in pressure, and equation 42 gives the overall uncertainty in pressure measurement.

$$\frac{\Delta P}{P} = \sqrt{\left(\frac{\Delta P_t}{P_t}\right)^2 + \left(\frac{\Delta v_p}{v_p}\right)^2} \tag{39}$$

$$\frac{\Delta P_t}{P_t} = 0.0025 \tag{40}$$

$$\Delta v = \pm 1.42\ mV \tag{41}$$

$$\frac{\Delta P}{P} = \sqrt{(0.0025)^2 + \left(\frac{1.42mV}{v_p}\right)^2} \tag{42}$$

6.1.3 Uncertainty in Area Measurement

Perhaps the most difficult quantity to measure in order to establish the nozzle coefficient of thrust is the nozzle throat area. Because the nozzle throat is internal to the nozzle geometry, it cannot be directly measured using calipers or other precision instruments. Instead, the nozzle throat area was measured using a set of precision plug gauges. The plug gauges are used to check for an interference fit with the nozzle throat, thus providing a measurement of the minimum diameter in the throat. The gauges are precision ground and provided by the manufacturer to a tolerance within 0.0001" of the specified diameter. The gauges were ordered in a set separated by 0.0005" (0.0127 mm) increments. After measuring the gauges with digital micrometers to confirm they met the specified tolerance, they were used to measure the throat diameters of the two printed nozzles. Both of the printed nozzles were found to have throat diameters between 0.0560" and 0.0565", or 1.422 mm and 1.435 mm. The uncertainty associated with this measurement can be estimated from the interval between plug gauges, or 0.0127 mm. The uncertainty associated with this measurement is $\pm 0.006\ mm$. The fractional uncertainty in diameter can then be expressed by equation 44. The fractional uncertainty in area can then be found from the uncertainty in diameter as shown in equation 46.

$$d_t = 1.429 \pm 0.006\ mm \tag{43}$$

$$\frac{\Delta d_t}{d_t} = \frac{0.006\ mm}{1.429\ mm} = \pm 0.0042 = \pm 0.42\% \tag{44}$$

$$A_t = \frac{\pi}{4} d_t^2 \tag{45}$$

$$\frac{\Delta A_t}{A_t} = 2\frac{\Delta d_t}{d_t} = \pm 0.0084 = \pm 0.84\% \tag{46}$$

6.1.4 Uncertainty in Coefficient of Thrust

Now the measurement uncertainty for the coefficient of thrust can be found by combining these contributing uncertainties according to equation 34, yielding equation 47 below.

$$\frac{\Delta C_\tau}{C_\tau} = \sqrt{\left(\frac{0.05N}{\tau}\right)^2 + \left(\frac{1.42mV}{v_\tau}\right)^2 + (0.0025)^2 + \left(\frac{1.42mV}{v_p}\right)^2 + \left(\frac{\Delta A_t}{A_t}\right)^2} \tag{47}$$

Equation 47 indicates that the uncertainty in thrust coefficient varies with the thrust and pressure observed for a given data point. This is because ΔF and Δv remain constant, while τ and v_τ vary, leading to a fractional uncertainty that varies with thrust and pressure.

In order to assess the precision and reliability of the coefficient of thrust data shown in figure 27, equation 47 was used to draw uncertainty bars on select data points (figure 28). Note that the pressure range shown in figure 28 is extends lower than in figure 27 in order to demonstrate the justification for only considering data above 375 psi. Also note that the machined nozzle represented by the lower data series is drawn in red for emphasis over the surrounding data.

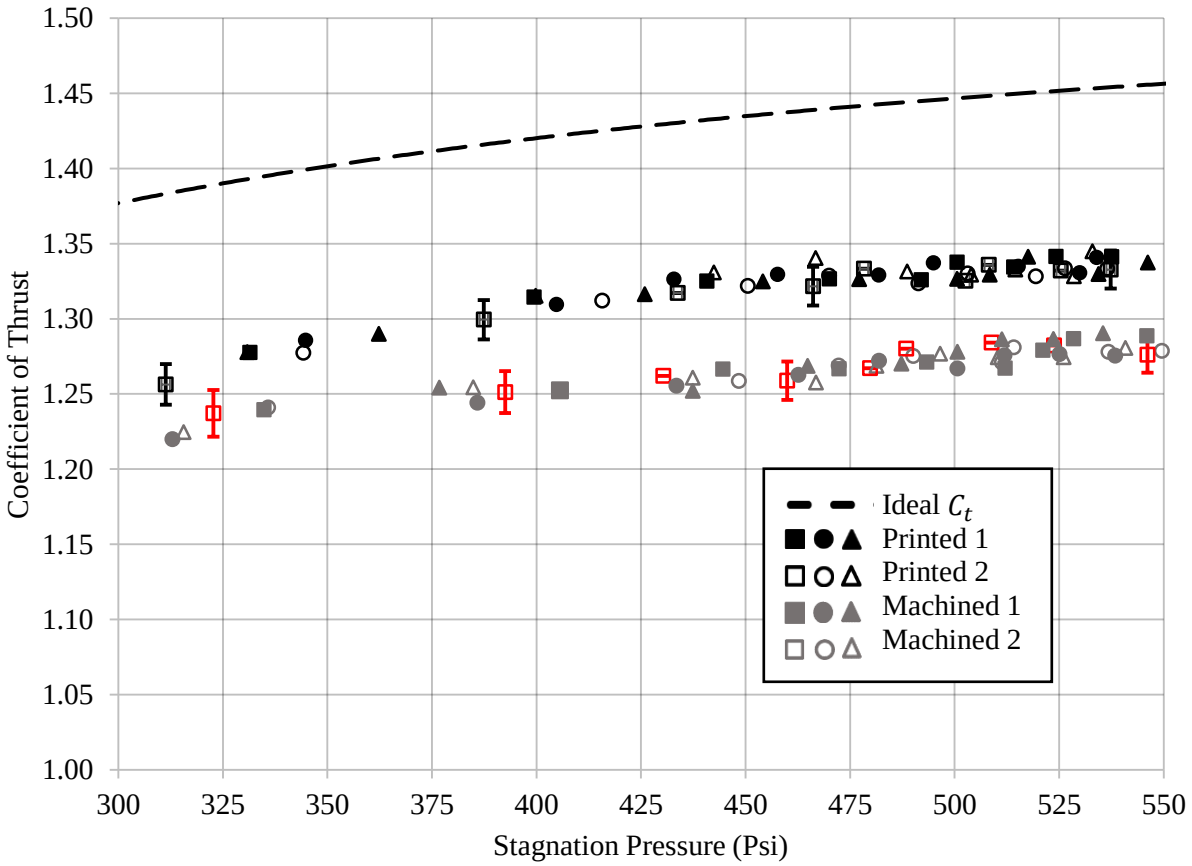

Figure 28: Uncertainty in experimental coefficient of thrust for RPT and machined nozzles

As shown in figure 28, the measurement uncertainty increases at lower stagnation pressures. The change in pressure also increases as the stagnation pressure decreases, resulting from the air tank approaching empty. This increased uncertainty and gap in available data justifies omitting data below 375 psia for a reliable performance comparison.

It is apparent that the printed nozzles performed more efficiently than the machined nozzles in all twelve tests conducted. To examine what underlying factors may cause this, the next section will focus on the mechanisms of thrust loss in nozzles and their estimated impact on the present results.

6.2 Nozzle Losses

At this point it is informative to examine the probable causes of deviations from the coefficient of thrust predicted by classical isentropic flow analysis. Taking the coefficient of thrust values at the design point of 450 psia, we find that the losses for the printed nozzles and machined nozzles are 8% and 12%, respectively. These losses represent deviations from the idealized assumptions made in the isentropic analysis conducted earlier. This section will identify and discuss probable loss mechanisms in an attempt to better understand nozzle performance and potential improvements that can be made.

6.2.1 Non-Axial Exit Velocity

The simplest factor to consider is that unlike de Laval or bell nozzles, the conical nozzle produces an exhaust jet that is not entirely axial. The losses due to non-axial exit velocity can be calculated using the well-known divergence relation, shown in equation 48 [16].

$$C_\theta = \frac{1 + \cos(\theta)}{2} \tag{48}$$

Where θ is the divergence half angle and $C_\theta$is a correction coefficient that is applied to the momentum thrust produced by the nozzle. Both the printed and machined nozzles diverge at a 10° half angle, giving a correction coefficient of 0.992. The total loss in thrust coefficient due to this effect is then 0.8%.

6.2.2 Nozzle Geometry

Another loss mechanism to consider is the effect of nozzle geometry. It is well established that sharp corners in sonic and supersonic flow can lead to the formation of shock waves, and consequently the loss of stagnation pressure and thrust. Isentropic flow equations assume an adequately smooth nozzle as to avoid these shock waves, but by examining the geometries of the two nozzles we find that the sharp corners in the machined nozzle are likely to lead to shocks.

In particular, the sharp angle between the converging section and throat is likely to lead to losses. To explain why, we must closely examine the gas dynamics in this region. As the flow reaches the throat from the converging section, the flow reaches Mach one. This sonic flow then encounters an abrupt expansion corner, leading to a Prandtl-Mayer expansion fan and supersonic flow beyond this corner. When this supersonic flow meets the nozzle center, it is forced to flow axially by the axisymmetric boundary condition, leading to the formation of a Mach reflection. This Mach reflection includes the formation of a Mach disk in the nozzle throat, which lowers the stagnation pressure and velocity of the flow that passes through it and lowers the thrust produced by the nozzle.

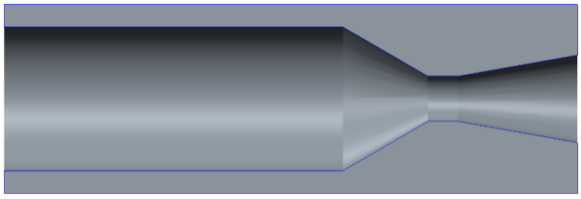

Figure 29: Machined nozzle with sharp corners

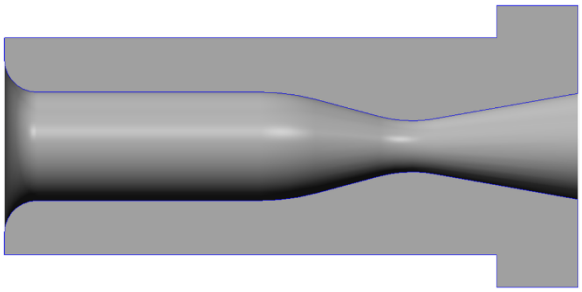

Figure 30: RPT nozzle with no sharp corners

In contrast, the printed nozzle has no such sharp angles and therefore does not lead to the formation of shocks. This effect is likely the most significant factor in explaining the performance gap between the printed and machined nozzles.

6.2.3 Reduced Mass Flux

The role of viscous effects in the performance of small nozzles is a current research topic that has seen increased interest in recent years. One effect of the viscous boundary layer is a reduction of effective throat area, leading to reduced mass flux. Although negligible in large nozzles, this effect becomes more important as nozzle size decreases. In 1978, Tang and Fennf published an expression for the discharge coefficient of adiabatic smooth-walled nozzles, which can be written as equation 49 [17].

$$C_d = 1 - \left(\frac{\gamma - 1}{2}\right)^{3/4} \left[3.266 - \frac{2.128}{\gamma + 1}\right] Re'^{-1/2} + 0.9428 \frac{(\gamma - 1)(\gamma + 2)}{(\gamma + 1)^{1/2}} Re'^{-1} \tag{49}$$

Where $Re'$is a modified Reynolds number accounting for throat curvature. The quantity Re' can be calculated by equation 50, where Re_t is the throat Reynolds number, R_t is the throat radius, and R_c is the radius of curvature in the throat.

$$Re' = Re_t \sqrt{R_t / R_c} \tag{50}$$

The throat Reynolds number can be calculated using known quantities by equation 51, taking care to evaluate the dynamic viscosity of the propellant using the throat conditions [18].

$$Re = \frac{\dot{m} d_t}{\mu A_t} \tag{51}$$

The mass flux can be estimated from the isentropic flow equations, noting that if the coefficient of discharge is significantly lower than unity a recalculation will be necessary. For stagnation conditions of 450 psia and 300K, we obtain a mass flow rate of 11.2 g/s. The static temperature at the throat can be calculated using the stagnation temperature expression (equation 10), which gives a temperature of 250K at the throat, corresponding to a dynamic viscosity of $1.599 * 10^{-5}$ kg/m-s. Plugging in, we find that the Reynolds number for the printed nozzle is 605,000. We then calculate the corrected Reynolds number (equation 50) using the radius of curvature of the nozzle throat, and find that $Re' = 2.97 * 10^{-5}$. Solving for the discharge coefficient, we find that $C_d = 0.995$.

Based on this analysis, the mass flux is reduced by 0.5% due to the throat boundary layer, corresponding to a 0.5% reduction in the coefficient of thrust. Although the reduced mass flux does lower the thrust produced by the nozzle, it will not negatively impact the specific impulse and is not a true loss in that respect.

6.2.4 Frictional Losses

One of the most difficult losses to analytically quantify is the loss due to viscous friction. The frictional losses depend on several factors including the geometry of the nozzle, wall heat flux, and local fluid properties. The wall surface roughness also effects the viscous friction due to the high Reynolds number and resulting turbulent flow. The analysis is further complicated by the interaction of the subsonic boundary layer and the supersonic freestream in the diverging portion of the nozzle. An experimental study conducted by NASA in 1965 acknowledges these difficulties and provides an empirical expression to estimate these losses (equation 52) [19].

$$C_f = 17.6 \exp\left(0.0032 \frac{A_e}{A_{th}}\right) Re_t^{-1/2} \tag{52}$$

Although this equation provides a means to estimate the viscous losses in our nozzle, the fit is based on testing of only six nozzles over a limited range of Reynolds numbers. Despite these limitations, we can

use this expression to obtain a rough estimate of the viscous losses expected for our case. Plugging in values for the printed nozzle, we find that the viscous loss is approximately 2.5%.

6.2.5 Surface Roughness

Surface roughness also plays a separate role in thrust loss for small nozzles. In addition to the effect of wall roughness on viscous loss, large surface roughness can also result in the formation of oblique shock waves in the throat and diverging nozzle sections. These shocks reduce the stagnation pressure available to the flow, as well as the flow velocity. Information on this loss mechanism is relatively rare in the literature. A recent study by [20] has examined this type of loss through the use of the commercial computational fluid dynamics (CFD) code FLUENT. The model incorporated several important physical phenomena, including varying fluid properties, shock formation and propagation, and viscous losses. The near wall interactions used approximations known in CFD as 'wall functions', which reduce the computational complexity of the simulation at the expense of accuracy in modeling the near wall region. The use of wall functions fails to capture the physical results of increased wall roughness, namely the perturbation of the flow and subsequent shock formation due to the presence of large extrusions from the wall. To complement the CFD study, [20] collected a small experimental data set as well. The results of the CFD and experimental studies were presented for various nozzle diameters, using normalized surface roughness as the independent variable (equation 53). The highest performing experimental nozzle was the 1 mm nozzle with 2 micron surface roughness ($\delta = 0.4\%$), which exhibited a 12% loss in thrust coefficient compared to theory. The CFD results for this case indicate a loss of under 4%. This discrepancy underscores the need for a reevaluation of the CFD approach, particularly in the near-wall region for accurate modeling of surface roughness losses.

$$\delta = \frac{R_{roughness}}{R_{throat}} \tag{53}$$

Although the CFD results do not match the experimental results for the small data set, a consistent trend for both CFD and experimental results show that as surface roughness increases, nozzle efficiency decreases. This result demonstrates that gains can be realized through surface treatment of nozzles to reduce the effective surface roughness.

6.2.6 Real Gas Effects

The assumption of ideal gas behavior is also a source of error in our ideal nozzle analysis. The validity of this assumption decreases as the gas approaches saturated conditions. We can estimate the error associated with this assumption using the compressibility factor (equation 54), which is a tabulated value that indicates deviation from ideal gas behavior. Table 6 shows the compressibility factor plotted for Nitrogen at five points in the diverging section of the nozzle [21]. Nozzle position x/L is equal to zero at the throat and one at the nozzle exit.

x/L	Diameter (mm)	Temp (K)	Pressure (Bar)	Compressibility Factor
0	1.50	250	16.2	0.986
0.2	1.78	184	5.6	0.982
0.4	2.06	157	3.2	0.979
0.6	2.34	139	2.1	0.981
0.8	2.62	125	1.4	0.983
1	2.90	113	1.0	0.984

Table 6: Compressibility factor at various points in the nozzle diverging section

$$Z = \frac{P}{\rho RT} \tag{54}$$

The compressibility factor shows a 1.5% to 2% deviation from ideal gas behavior throughout the diverging section. It is difficult to assess the exact effect this deviation will have on nozzle performance without the use of a computer code accounting for real gas behavior. Considering the density at the nozzle throat (equation 56), we find that the actual mass flux should be approximately 1.4% higher than the value predicted by the ideal gas law. This correction will increase the ideal thrust coefficient by 1.4%.

$$\rho = \frac{1}{Z}\frac{p}{RT} \tag{55}$$

$$\rho_{t,actual} = \frac{1}{0.986}\rho_{t,ideal} = 1.014\,\rho_{t,ideal} \tag{56}$$

6.2.7 Other Losses

Additional losses that are typically included in a nozzle efficiency analysis include wall heat flux and erosion of the nozzle throat. Typically in a hot flow scenario, heat loss to the nozzle walls through both convection and radiation can degrade performance. In the case of a cold gas thruster, however, the gases flowing through the nozzle are colder than the nozzle walls, and any heat exchange with the walls would tend to increase the performance of the nozzle. Additionally, the nozzle walls are made of a material with a low thermal conductivity, which will tend to minimize heat exchange between the walls and propellant. Similarly, erosion of the nozzle throat is expected to occur in high temperature rockets only. The nozzle throat measurements were checked before and after testing to confirm that no measurable erosion had occurred.

6.2.8 Nozzle Loss Summary

The loss mechanisms discussed in the previous sections are summarized in table 7, along with the estimated losses from these effects. The primary causes of loss in thrust coefficient compared to the ideal value can be attributed to a combination of viscous friction and surface roughness. The effects of surface roughness on losses in small nozzles is an ongoing research topic that has received increased attention as additive manufacturing has grown in popularity, and is likely the single largest contributor to losses in this study.

Cause	Estimated Change	Reference
Non-axial exit velocity	-0.76%	[16]
Reduced mass flux due to throat boundary layer	-0.50%	[17,22]
Viscous friction	-2.5%	[19]
Surface roughness	-3%-5%	[20]
Real gas effects	+1.4%	[21]

Table 7: Summary of sources of error in the ideal isentropic flow analysis for printed nozzle

The constant loss related to non-axial exit velocity is a simple result of the conical nozzle geometry, and can easily be overcome by 3D printing a de Laval or bell shaped nozzle. The viscous reduction in mass flux is a direct result of the nozzle scale and size of the boundary layer in the nozzle throat. Although this 'loss' reduces the coefficient of thrust for the nozzle, it does not affect the specific impulse and therefore does not need to be mitigated for improved nozzle performance.

Figure 31 shows the coefficient of thrust results for the printed and machined nozzles corrected for non-axial exit velocity, reduced mass flux due to throat boundary layer, and real gas effects. The remaining losses are shown in red arrows on the plot below. The arrow labeled "1" indicates the roughly 7% loss for the printed nozzle due to viscous friction and surface roughness. The arrow labeled "2" indicates the roughly 12% loss for the machined nozzle due to nozzle geometry, viscous friction, and surface roughness. The indicated losses for both nozzles may be mitigated through the proper contouring of the nozzle, and through treatments to reduce the nozzle surface roughness.

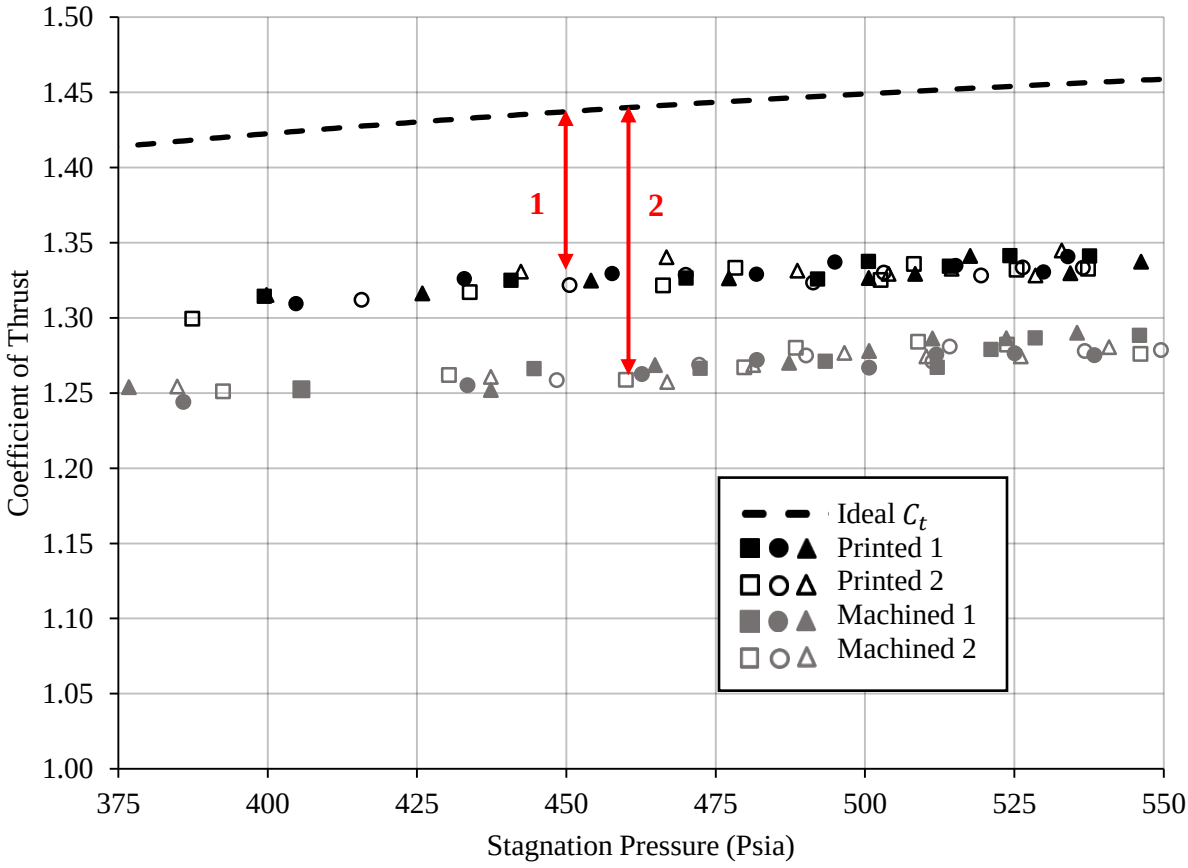

Figure 31: Coefficient of thrust corrected for non-axial exit velocity, reduced mass flux, and real gas effects. Arrows labeled (1) and (2) show the remaining losses for the RPT nozzles and machined nozzles, respectively.

CHAPTER 7

CONCLUSIONS

Additive manufacturing is a powerful fabrication tool that has become increasingly affordable and available in recent years. The ability to produce scalable nozzles to fit a wide range of applications is especially useful in fabricating small nozzles that are prohibitively difficult to machine. Although several groups have fabricated nozzles through additive manufacturing, relatively little data is available regarding the performance of these nozzle compared to traditionally machined nozzles. Furthermore, what little information is available focuses on nozzles manufactured by laser sintering as opposed to methods used by widely available consumer 3D printers. This study addresses this deficiency through extensive testing of rapid prototyped nozzles manufactured using a low-cost consumer 3D printer. It was shown that for small dimensions, printed nozzles outperformed machined nozzles, showing 7% and 12% losses compared to theory, respectively.

In addition to conducting a performance comparison, nozzles were designed for an application in attitude control for low-altitude rocketry. The systematic design, sizing, and performance analysis of nozzles is discussed in sufficient detail for readers to reproduce this process for alternative applications. The use of rapid prototyping over traditional machining in nozzle fabrication allows improved scalability of nozzles, and greatly reduces manufacturing costs as well. Further applications for rapid prototyped nozzles includes small satellites in need of propulsion for guidance and control capabilities, or in providing such capabilities to other low-cost spacecraft. The structural integrity of nozzles was also evaluated and rapid prototyped nozzles were shown to be sufficiently robust, holding pressure and producing the same thrust after multiple tests.

Rapid prototyped nozzles have been shown to be a competitive alternative to machining or laser sintering for small nozzles. Rapid prototyped nozzles were shown to outperform machined nozzles, as well as maintain structural integrity and durability over multiple tests. This manufacturing method can deliver improved capability and reduced cost as compared to traditional machining, and is widely available in Universities and small companies.

Extensions to this work would most likely focus on quantifying the surface roughness of rapid prototyped and machined nozzles. Since a wide range of manufacturing techniques can be used to rapid prototype parts, it is likely that the methodology for nozzle fabrication used in this study can be improved. Post processing techniques may also provide decreased surface roughness and improved performance. Another important research topic is the comparison of RPT nozzles to those produced using SLS or SLM additive manufacturing techniques. As the body of literature on AM propulsion systems grow, conclusions can likely be drawn by comparing the findings of this study to similar studies on the performance of propulsion systems producing using SLS or SLM techniques.

REFERENCES

1. Quigley, N., & Lyne, J. E. (2014). Development of a three-dimensional printed, liquid-cooled nozzle for a hybrid rocket motor. *Journal of Propulsion and Power*. Vol. 30, No. 6 (2014), pp 1726-1727.
2. Gradl, P. R., Greene, S. E., Protz, C. S., Ellis, D. L., Lerch, B., & Locci, I. E. (2017, July). Development and Hot-fire Testing of Additively Manufactured Copper Combustion Chambers for Liquid Rocket Engine Applications. In *53rd AIAA/SAE/ASEE Joint Propulsion Conference*, Paper No. AIAA 2017-4670.
3. Gagne, K. R., Hitt, D. L., & McDevitt, M. R. (2016). Development of an additively manufactured microthruster for nanosatellite applications. In *54th AIAA aerospace sciences meeting*, Paper No. AIAA 2016-0963.
4. Schmidt, E., Louke, J., Arnell, K., Hickman, J., & Wiles, B. (2015). Development of a Low-Cost, Open-Hardware Attitude Control System for High-Powered Rockets. In *AIAA SPACE 2015 Conference and Exposition*, Paper No. AIAA 2015-4623.
5. Stevenson, T. H. (2015). *Design and testing of a 3D printed propulsion system for small satellites* (Doctoral dissertation), University of Texas at Austin.
6. FormLabs website, www.formlabs.com/3d-printers/form-2/.
7. Palmer, M. J., Roberts, G. T., & Musker, A. J. (2011). Design, build and test of a 20N hydrogen peroxide monopropellant thruster. AIAA Paper No 2011-5697.
8. Polk, J. E., Pancotti, A., Haag, T., King, S., Walker, M., Blakely, J., & Ziemer, J. (2013). Recommended practices in thrust measurements. No. IEPC-2013-440. California Institute of Technology Pasadena Jet Propulsion Lab.
9. Xing, Q., Zhang, J., Qian, M., Jia, Z., & Sun, B. (2011). Design, calibration and error analysis of a piezoelectric thrust dynamometer for small thrust liquid pulsed rocket engines. Measurement, 44(2), 338-344.
10. Cervone, A., Torre, L., d'Agostino, L., Musker, A. J., Roberts, G. T., Bramanti, C., & Saccoccia, G. (2006). Development of hydrogen peroxide monopropellant rockets. Paper No. AIAA 2006-5239.
11. Seitzman, Jerry. (2006). Rocket propulsion: thrust coefficient, characteristic velocity and ideal nozzle expansion. Georgia Tech AE4451 class notes.
12. Anderson, J. D. (1990). Modern compressible flow: with historical perspective (Vol. 12). New York: McGraw-Hill.
13. Meyers, J. M. Nozzle thermodynamics and isentropic flow relations. University of Vermont ME239 class notes.
14. Assad Anis (2012). Cold Gas Propulsion System - An Ideal Choice for Remote Sensing Small Satellites, Remote Sensing - Advanced Techniques and Platforms, Dr. Boris Escalante (Ed.), InTech, DOI: 10.5772/37149. Available from: https://www.intechopen.com/books/remote-sensing-advanced-techniques-and-platforms/cold-gas-propulsion-system-an-ideal-choice-for-remote-sensing-small-satellites.
15. Back, L. H., Cuffel, R. F., & Massier, P. F. (1969). Transonic flowfield in a supersonic nozzle with small throat radius of curvature. *AIAA Journal*, *7*(7), 1364-1366.
16. Berton, J. J. (1991). Divergence thrust loss calculations for convergent-divergent nozzles: Extensions to the classical case. NASA Technical Memorandum, 105176, 7.
17. Fennf, J. B. (1978). Experimental determination of the discharge coefficients for critical flow through an axisymmetric nozzle, *AIAA Journal*, Vol. 16, No. 1, pp. 41-46.

18. Louisos, W. F., & Hitt, D. L. (2012). Viscous Effects on Performance of Three-Dimensional Supersonic Micronozzles. Journal of Spacecraft and Rockets, 49(1), 51-58.
19. Spisz, E. W., Brinich, P. F., & Jack, J. R. (1965). Thrust coefficients of low-thrust nozzles. National Aeronautics and Space Administration Cleveland OH Lewis Research Center, Paper No. NASA-TN-D-3056.
20. Cai, Y., Liu, Z., & Shi, Z. (2017). Effects of dimensional size and surface roughness on service performance for a micro Laval nozzle. Journal of Micromechanics and Microengineering, 27(5), 055001.
21. Green, D. W., & Perry, R. H. (1999). Perry's chemical engineers' handbook.
22. Seitzman, Jerry. (2012). Losses and real nozzle effects. Georgia Tech AE6450 class notes.

APPENDIX A: Analog Instrumentation Circuitry

The nozzles to be tested have approximate throat diameters of 1.5 mm and a design stagnation pressure of 450 psia. In order to study nozzle performance in both over and underexpanded conditions, the nozzles will be tested up to 600 psia. The range of thrust to be measured is therefore based on the expected thrust at this stagnation pressure. Applying the predictions from section 3, we expect to see a peak thrust around 10N during testing. In order to provide some overhead in measurement range, especially considering the transient dynamic loads that may be experienced due to vibration, a thrust range of 0-15N was chosen as an appropriate range. Also, since accurate measurement of the quasi-steady thrust is of principal importance, a strain gauge based load cell was chosen over a faster responding piezoelectric sensor. An Omega LCEB-10 load cell was chosen based on these requirements. The LCEB-10 uses a full Wheatstone bridge to provide a 0-30 mV signal over a range of 0-44N (0-10 lbf).

Signal conditioning for the load cell was provided by analog circuitry designed to amplify the measured signal to match the input range of the DAQ board, and to reject radio frequency interference from the signal path. The conditioning circuit, shown in figure 32, is built around a rail to rail instrumentation class amplifier (Analog Devices AD623B) with extremely low nonlinearity and good common mode rejection (table 8).

Gain Range	$1 - 1000$
Nonlinearity	$50\ ppm$
Gain vs. Temperature	$50\ ppm/°C$
Input Impedance	$2\ G\Omega, 2\ pF$
Common Mode Rejection at 60 Hz	$110\ dB$
Input Bias Current	$17\ nA$

Table 8: Instrumentation amplifier specifications

The first AD623 in the circuit removes the bias from the load cell, centering the common mode voltage around the ground reference. This allows the output of the second AD623 to range from the negative supply voltage to the positive supply voltage (-5V to +5V). The second AD623 amplifies the millivolt signal from the LCEB-10 load cell to match the -5V to +5V input range of the DAQ board, maximizing the resolution of measurement. The desired measurement range of 0-15N will produce a 0-10 mV swing from the load cell. Leaving approximately one volt on either side of the -5V to +5V range in order to prevent saturation of the instrumentation amplifier, the required gain to amplify a 10mV signal to 8V is a gain of 800. Referring to the AD623 datasheet, this gain is achieved by using a 125 ohm gain resistor.

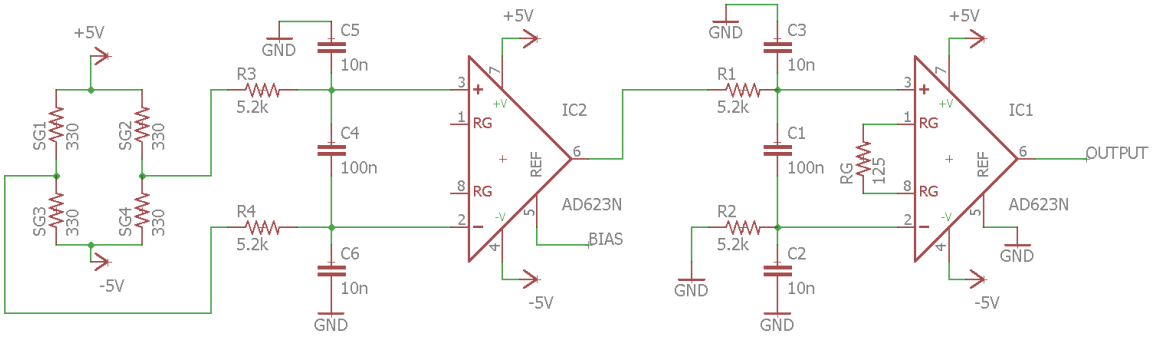

Figure 32: Signal conditioning and amplification circuit for thrust measurement

The millivolt signal from the load cell is carried by a twisted pair of wires in order to ensure that the electrical interference picked up by both wires is nearly identical, and thus appears as a common mode voltage at the amplifier. The wire is also shielded with a conductor surrounding both wires to further reduce the effects of electrical interference. To further mitigate the effects of electrical interference, a set of low pass filters were placed at the inputs of each instrumentation amplifier. Following the recommendations for radio frequency isolation listed on the AD623 datasheet, the filters consist of two resistors and three capacitors each. At the inputs of the first instrumentation amplifier, a low pass filter formed by R3/C5 and R4/C6 attenuates common mode signals produced by electrical interference. The cutoff frequency for this filter was selected to reject 99.5% of the common mode signal from the amplifier output. Referring to the AD623 datasheet for a gain of one, it can be seen that at above 3kHz the common mode rejection ratio falls below 65dB (99.5%), and as such the cutoff frequency of the common mode low pass filter was set at 3kHz. The capacitor C4 is necessary to preserve the common mode rejection at frequencies near or below the common mode cutoff frequency. This is because any mismatch in the cutoff frequency between the R3/C5 and R4/C6 pairs will cause the common mode signal to be converted to a differential signal at some frequencies. The capacitor C4 rejects this differential signal by having a substantially lower cutoff frequency for differential signals. The size of the C4 capacitor was selected based on recommendations from the AD623 datasheet, stating that the differential capacitor should be approximately ten times the size of the common mode capacitors. This gives a differential cutoff frequency of 160 Hz.

In order to provide a solid contact between the load cell and the moving platform of the thrust stand, the leaf springs on the thrust stand are used to place a small preload on the load cell prior to experimentation. This preload helps to provide good contact with the load cell during thrust measurement, but introduces a bias that must be removed prior to signal amplification. The first instrumentation amplifier in the thrust signal conditioning circuit serves to remove this bias by subtracting a bias reference voltage from the transducer output. This bias voltage is provided by a simple voltage divider buffered by an Analog Devices AD8067 operational amplifier (figure 33).

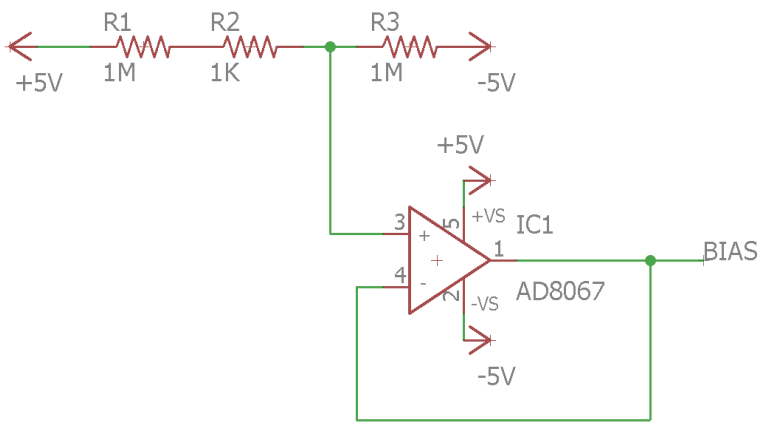

Figure 33: Voltage divider circuit for thrust bias signal

The voltage divider provides -5 mV to the input of the operational amplifier, which is configured as a voltage follower. This amplifier matches this -5 mV input, while providing a low impedance output to the reference pin of the AD623 instrumentation amplifier. This configuration ensures that the bias voltage remains constant regardless of the current draw of the instrumentation amplifier reference pin.

The -5V and +5V supply rails for the measurement circuit are provided by fixed output linear voltage regulators (Texas Instruments μA79M05C and National Semiconductor LM140, respectively). Linear regulators were chosen over more efficient switching regulators due to their superior stability in output voltage. Two 9V batteries deliver a steady supply of power to the voltage regulators free of 60Hz noise often introduced by grid powered power supplies. In combination with the low dropout voltages provided by the voltage regulators, the smooth battery supply and good line and load regulation of the regulators ensures a steady power supply to the signal conditioning circuitry for precise measurements.

Output Voltage	5V
Output Current	1A
Input Voltage	7.5V – 20V
Line Regulation	10mV
Load Regulation	10mV

Table 9: LM340 voltage regulator specifications

Output Voltage	-5V
Output Current	500mA
Input Voltage	-7.5V – -20V
Line Regulation	7mV
Load Regulation	50mV

Table 10: uA79M00 voltage regulator specifications

Nozzle plenum pressure was measured using an Omega PX309 pressure transducer. This transducer measures pressures in the range of 0-1000 psig and outputs a signal from 0-100 mV. The transducer has a bandwidth of over 1 kHz, considerably higher than the resonant frequency of the system and capable of recording pressure transients that may be correlated with thrust data. The expected pressure range during testing is 0-600 psig, yielding a 0-60 mV signal from the pressure transducer. Since this voltage range is considerably higher than the 0-10 mV range from the load cell, less complex circuitry is needed to condition the signal and maintain noise within an acceptable threshold. For this reason, the measurement circuitry for the pressure transducer (figure 34) is less complex than the circuitry for the load cell.

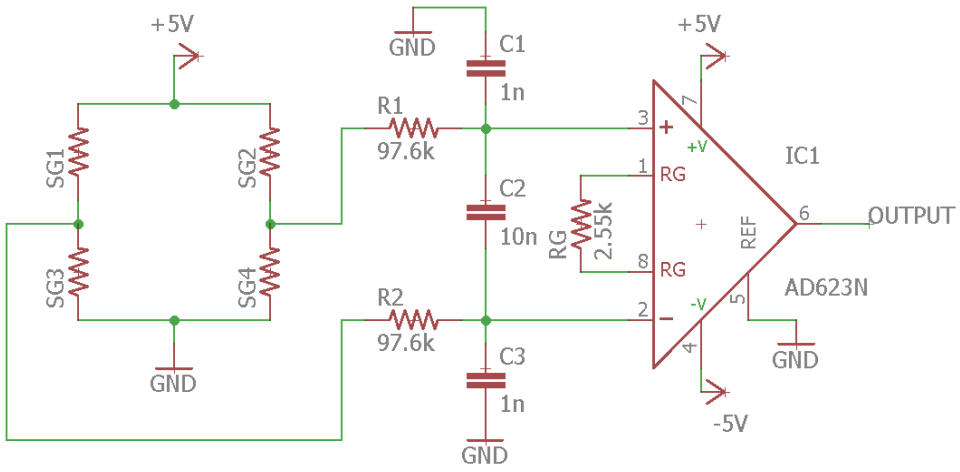

Figure 34: Signal conditioning and amplification circuit for pressure measurement

The measurement circuitry for the pressure transducer uses the same architecture as the load cell circuit, but uses a single AD623 instrumentation amplifier for signal amplification. Since the pressure transducer uses a 5V excitation voltage, the common mode signal from the transducer is $V_{CM} = 2.5\,V$. Referring to figure 21 of the AD623 datasheet, the maximum output of the amplifier is around 3.5 V under these conditions. In order to provide overhead and prevent saturation of the amplifier during testing, the pressure range that can be measured prior to saturation will be 0-850 psig, corresponding to a 0-85 mV signal from the transducer. In order to match the transducer signal to the 0-3.5V output range of the instrumentation amplifier, a gain of 40 was selected.

Similar to the load cell circuit, the pressure measurement circuit includes a low pass filter network to reject electrical interference prior to the amplifier inputs. The resistors R1 and R2 were sized to be sufficiently higher than the output resistance of the pressure transducer to prevent affecting the transducer output, but not so large as to substantially increase the thermal noise in the signal. The common mode cutoff frequency was set to 1.6 kHz and the differential cutoff frequency is 80 Hz. These filters will not affect the measured signal above the system resonant frequency, but serve to reduce the effects that electrical noise will have on the measured values.

APPENDIX B: Thrust Stand Vibration Analysis

In order to establish a limit for thrust measurement bandwidth, a series of vibration tests were conducted. These tests consisted of "tapping" the nozzle and other locations on the moving platform of the thrust stand to apply an impulse load, and measuring the resulting thrust response. Tap testing is common practice in structural analysis and can be used to find the frequency response of a structure. Figure 35 shows a representative thrust response to an impulse load. The x-axis shows elapsed time since the impulse was applied. For this test, the load cell signal was directly measured rather than using the analog circuitry for conditioning and amplification in order to avoid problems with amplifier saturation.

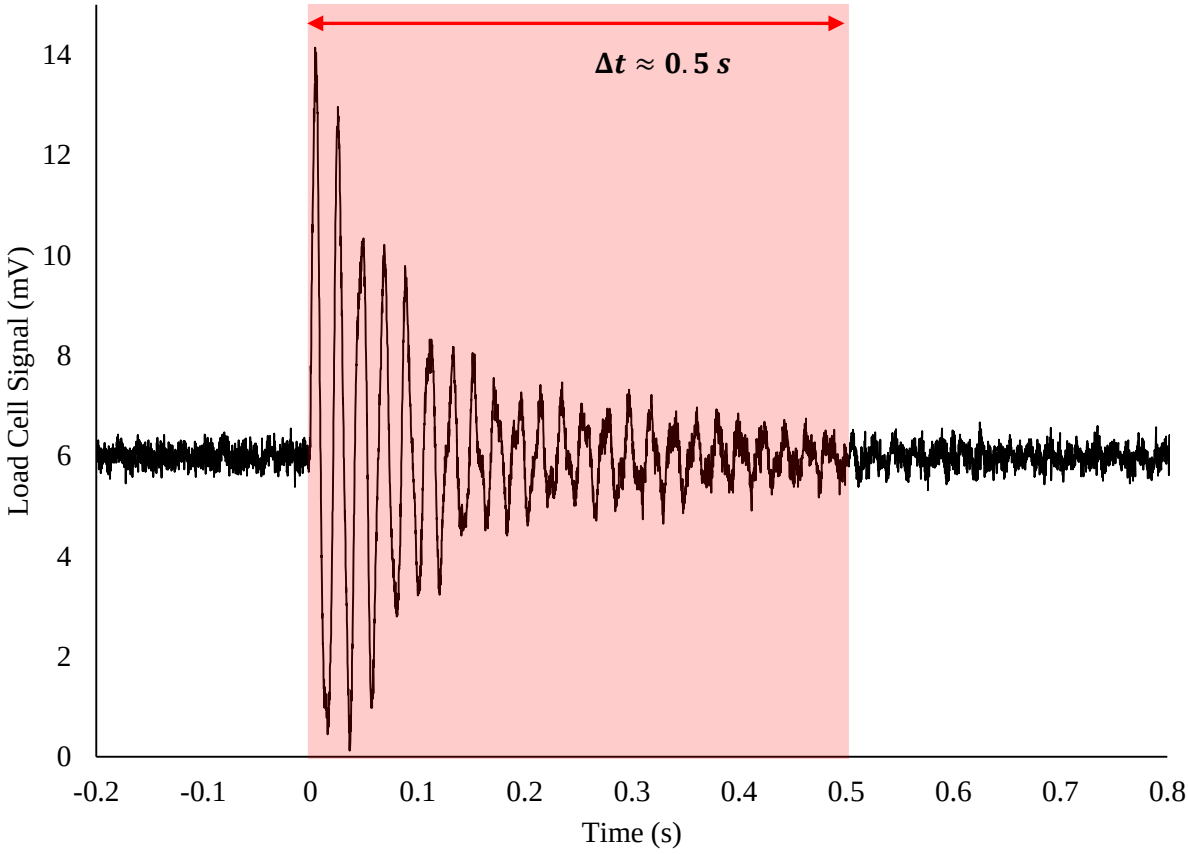

Figure 35: Measured thrust response to tap test (impulse response)

The thrust data shows a noise floor of approximately 0.5 mV due to electromagnetic interference from the surroundings. Since the signal conditioning circuit is not used, the high frequency interference is not filtered out and appears in the signal. The tap response shows a clear frequency component, corresponding to the natural frequency of the thrust stand. The response decays by 90% after approximately 0.5 seconds. In order to better identify the frequencies present in the signal, a Fourier transform (FFT) was performed on the data to obtain figure 36. Two obvious peaks appear in the FFT at 48.5 Hz and 110 Hz, the former corresponding the fundamental resonant frequency of the thrust stand.

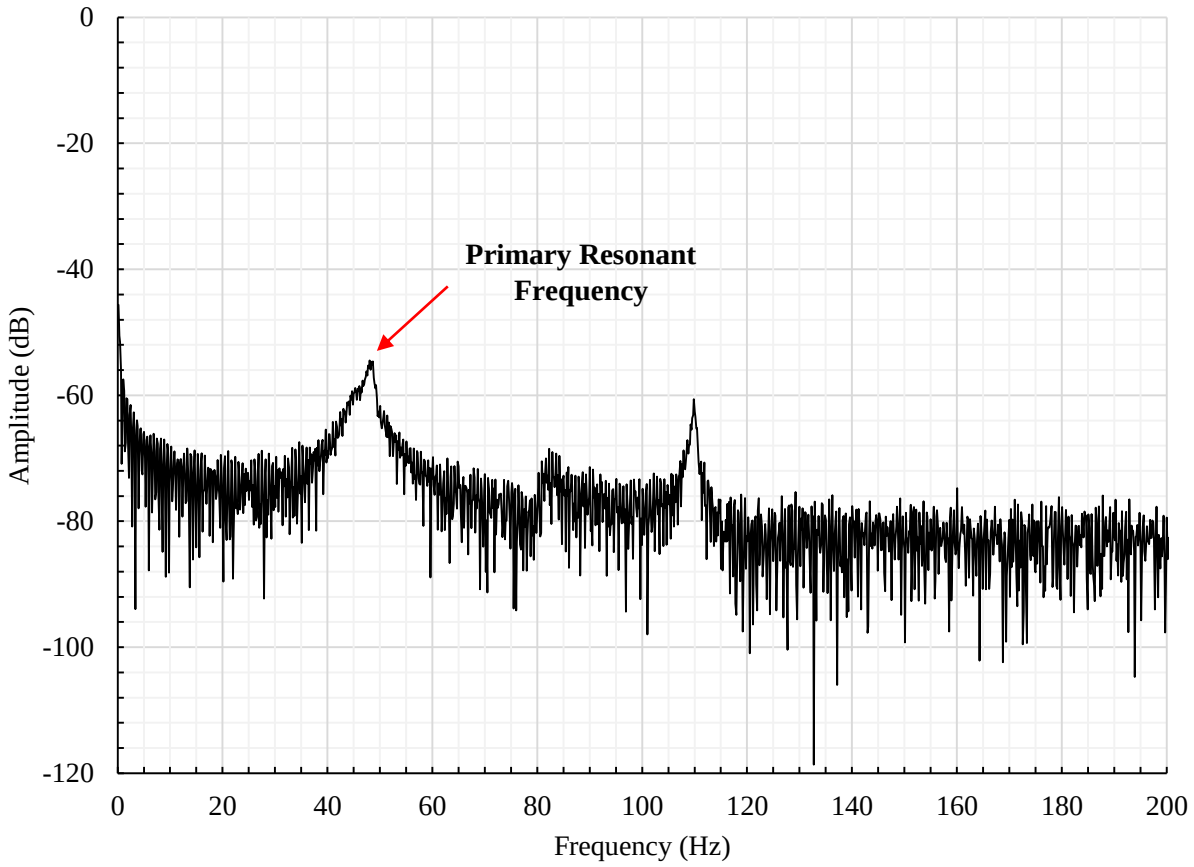

Figure 36: Fourier transform (FFT) of thrust stand impulse response showing resonance at 48.5 Hz and 110 Hz

Now that the frequency response function has been found by performing an FFT on impulse response data, the accurate measurement bandwidth can be found by looking more closely at the fundamental frequency. Figure 37 shows the frequency response replotted with the y-axis on a linear scale and normalized by the response amplitude at the resonant frequency. The full width at half maximum (FWHM) characterizes the range of frequencies over which the frequency response is at least half the amplitude of the response at the resonant frequency. In this case the FWHM is 1.68 Hz, meaning that the response amplitude drops to half of the resonant response at 0.84 Hz below the resonant frequency. Using three times the FWHM value as a cutoff, we find that the thrust measurement bandwidth is 0 Hz to 46 Hz.

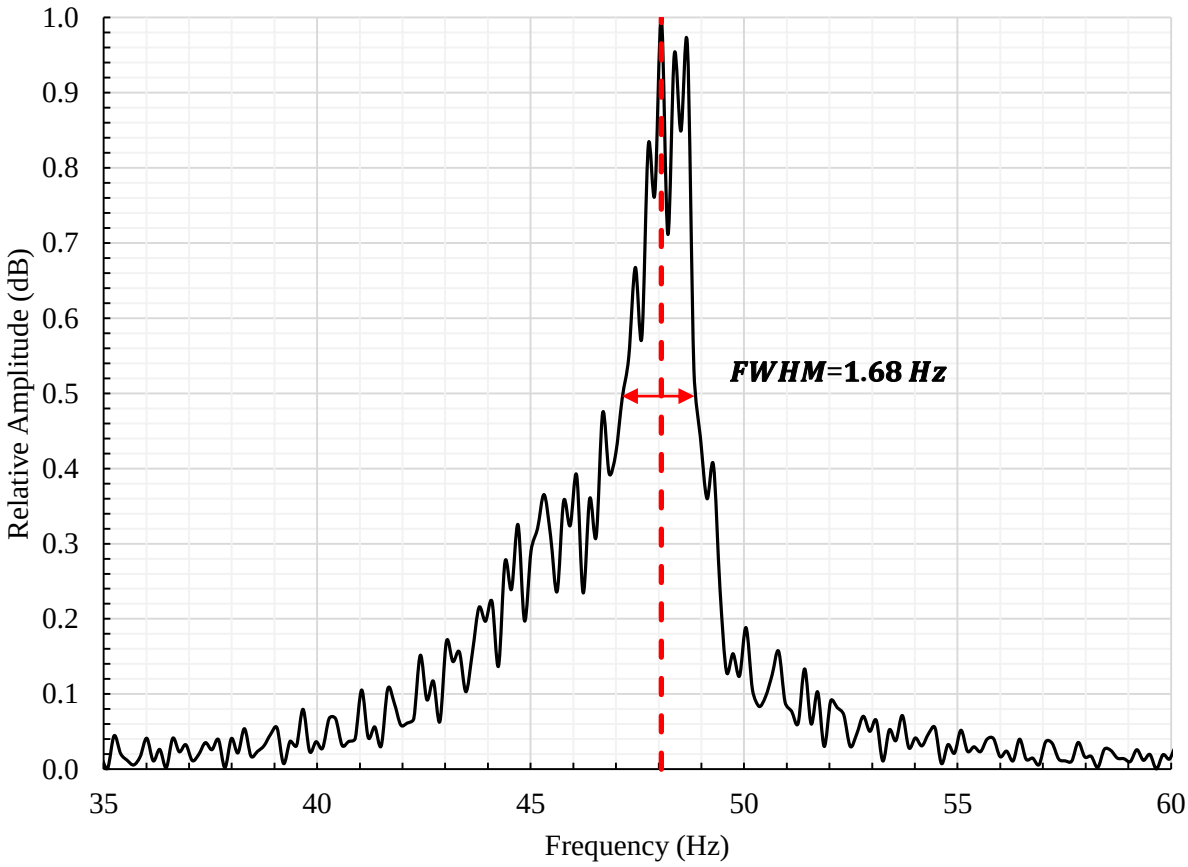

Figure 37: FFT normalized by response at resonant frequency showing the Full Width at Half Max (FWHM)